

# Gemini NIFS survey of feeding and feedback processes in nearby active galaxies – I. Stellar kinematics

Rogemar A. Riffel,<sup>1</sup>★ Thaisa Storchi-Bergmann,<sup>2</sup> Rogerio Riffel,<sup>2</sup>  
Luis G. Dahmer-Hahn,<sup>2</sup> Marlon R. Diniz,<sup>1</sup> Astor J. Schönell<sup>2</sup>  
and Natacha Z. Dametto<sup>2</sup>

<sup>1</sup>*Departamento de Física, Centro de Ciências Naturais e Exatas, Universidade Federal de Santa Maria, 97105-900 Santa Maria, RS, Brazil*

<sup>2</sup>*Departamento de Astronomia, Instituto de Física, Universidade Federal do Rio Grande do Sul, CP 15051, 91501-970 Porto Alegre, RS, Brazil*

Accepted 2017 May 24. Received 2017 May 18; in original form 2016 November 21

## ABSTRACT

We use the Gemini Near-Infrared Integral Field Spectrograph (NIFS) to map the stellar kinematics of the inner few hundred parsecs of a sample of 16 nearby Seyfert galaxies, at a spatial resolution of tens of parsecs and spectral resolution of 40 km s<sup>−1</sup>. We find that the line-of-sight (LOS) velocity fields for most galaxies are well reproduced by rotating disc models. The kinematic position angle (PA) derived for the LOS velocity field is consistent with the large-scale photometric PA. The residual velocities are correlated with the hard X-ray luminosity, suggesting that more luminous active galactic nuclei have a larger impact in the surrounding stellar dynamics. The central velocity dispersion values are usually higher than the rotation velocity amplitude, what we attribute to the strong contribution of bulge kinematics in these inner regions. For 50 per cent of the galaxies, we find an inverse correlation between the velocities and the  $h_3$  Gauss–Hermite moment, implying red wings in the blueshifted side and blue wings in the redshifted side of the velocity field, attributed to the movement of the bulge stars lagging the rotation. Two of the 16 galaxies (NGC 5899 and Mrk 1066) show an S-shape zero velocity line, attributed to the gravitational potential of a nuclear bar. Velocity dispersion ( $\sigma$ ) maps show rings of low- $\sigma$  values ( $\sim 50$ – $80$  km s<sup>−1</sup>) for four objects and ‘patches’ of low  $\sigma$  for six galaxies at 150–250 pc from the nucleus, attributed to young/ intermediate age stellar populations.

**Key words:** galaxies: active – galaxies: ISM – galaxies: kinematics and dynamics – infrared: galaxies.

## 1 INTRODUCTION

Active galactic nuclei (AGNs) characterize a critical phase in galaxy evolution in which its nuclear supermassive black hole (SMBH) is being fed due to gas accretion to the nuclear region. Once the accretion disc surrounding the SMBH is formed, feedback processes begin to occur, comprising jets of relativistic particles emitted from the inner rim of the accretion disc, winds emanating from outer regions of the disc and radiation emitted by the hot gas in the disc or by its corona (Elvis 2000; Frank, King & Raine 2002; Ciotti et al. 2010). The AGN feeding and feedback processes couple the growth of the SMBHs and their host galaxies, and are claimed to explain the correlation between the mass of the SMBH and the mass of the galaxy bulge (Ferrarese & Ford 2005; Somerville et al. 2008; Kormendy & Ho 2013). The feeding processes are a necessary con-

dition to trigger the nuclear activity, while the feedback processes are now a fundamental ingredient in galaxy evolution models: without the AGN feedback, the models cannot reproduce the properties of the massive galaxies – these galaxies end up forming too many stars (Springel et al. 2005; Fabian 2012; Terrazas et al. 2016).

The study of feeding and feedback processes in AGNs requires a detailed mapping of the gas and stellar kinematics in the vicinity of the central engine. Usually these studies are based on high-spatial resolution integral field spectroscopy (IFS; e.g. Fathi et al. 2006; Storchi-Bergmann et al. 2007, 2009, 2010; Barbosa et al. 2009, 2014; Hicks et al. 2009, 2013; Sánchez et al. 2009; Riffel & Storchi-Bergmann 2011a; Riffel et al. 2013; Mazzalay et al. 2014; Riffel et al. 2014; Schönell et al. 2014; Diniz et al. 2015; Fischer et al. 2017). To isolate and quantify gas streaming motions towards the centre of galaxies or gas outflows from the nucleus through the gas kinematics, it is necessary to properly map the motions of the gas due to the gravitational potential of the galaxy. A way to map the gravitational potential of the galaxies is by two-dimensional

\* E-mail: rogemar@ufsm.br

**Table 1.** Sample: (1) galaxy's name; (2) redshift; (3) nuclear activity; (4) Hubble type as quoted in NED; (5) spectral resolution in Å; (6) angular resolution; (7) spectral band; (8) Gemini project code; (9) total exposure time; (10) hard X-ray luminosity (14–195 keV) from the *Swift*-BAT 60-month catalogue (Ajello et al. 2012); (11) reference for the stellar kinematics.

1	2	3	4	5	6	7	8	9	10	11
Galaxy	$z$	Act.	Hub. type	Sp. R.	An. R. (arcsec)	B	Project ID	Exp. T.	$\log L_X$ (erg s <sup>-1</sup> )	Ref.
NGC788	0.014	Sy2	SA0/a?(s)	3.5	0.13	<i>K</i>	GN-2015B-Q-29	4400	43.2	a
NGC1052 <sup>a</sup>	0.005	Sy2	E4	3.4	0.14	<i>K1</i>	GN-2010B-Q-25	2400	41.9	a
NGC2110	0.008	Sy2	SAB0 <sup>-</sup>	3.4	0.15	<i>K1</i>	GN-2010B-Q-25	3600	43.3	b
NGC3227	0.004	Sy1.5	SAB(s)a pec	3.4	0.13	<i>K1</i>	GN-2016A-Q-6	2400	42.3	a
NGC3516	0.009	Sy1.5	(R)SB0 <sup>0</sup> ?(s)	3.6	0.15	<i>K</i>	GN-2015A-Q-3	4500	42.7	a
NGC4051 <sup>a</sup>	0.002	Sy1	SAB(rs)bc	3.2	0.17	<i>K</i>	GN-2006A-SV-123	4500	41.5	c
NGC4235	0.008	Sy1	SA(s)a edge-on	3.4	0.13	<i>K1</i>	GN-2016A-Q-6	4000	42.3	a
NGC4388	0.008	Sy2	SA(s)b? edge-on	3.5	0.14	<i>K</i>	GN-2015A-Q-3	800	43.3	a
NGC5506	0.006	Sy1.9	Sa pec edge-on	3.5	0.15	<i>i</i>	GN-2015A-Q-3	4000	43.1	a
NGC5548 <sup>a</sup>	0.017	Sy1	(R')SA0/a(s)	3.5	0.20	<i>K1</i>	GN-2012A-Q-57	2700	43.4	a
NGC5899 <sup>a</sup>	0.009	Sy2	SAB(rs)c	3.5	0.12	<i>K1</i>	GN-2013A-Q-48	4600	42.1	a
NGC5929 <sup>a</sup>	0.008	Sy2	Sab? pec	3.2	0.12	<i>K1</i>	GN-2011A-Q-43	6000	–	d
Mrk607 <sup>a</sup>	0.009	Sy2	Sa? edge-on	3.5	0.12	<i>K1</i>	GN-2012B-Q-45	6000	–	a
Mrk766	0.013	Sy1.5	(R')SB(s)a?	3.5	0.19	<i>K1</i>	GN-2010A-Q-42	3300	42.8	a
Mrk1066 <sup>a</sup>	0.012	Sy2	(R)SB0 <sup>+</sup> (s)	3.3	0.15	<i>K1</i>	GN-2008B-Q-30	4800	–	e
Mrk1157 <sup>a</sup>	0.015	Sy2	(R')SB0/a	3.5	0.12	<i>K1</i>	GN-2009B-Q-27	3300	–	f

<sup>a</sup>These galaxies do not follow all selection criteria and are part of the complementary sample.

a – This work; b – Diniz et al. (2015); c – Riffel et al. (2008); d – Riffel, Storchi-Bergmann & Riffel (2015c); e – Riffel & Storchi-Bergmann (2011a);

f – Riffel & Storchi-Bergmann (2011b).

mapping of the stellar kinematics. So far, studies available for nearby galaxies show that the stellar kinematics usually present regular rotation within the inner kiloparsec (e.g. Barbosa et al. 2006; Ganda et al. 2006) and thus can be used to isolate possible non-circular motions from the gas kinematics (e.g. Riffel et al. 2008; Riffel & Storchi-Bergmann 2011a; Diniz et al. 2015).

Adaptive optics IFS at 10-m class telescopes provides an unprecedented possibility to map the stellar kinematics of nearby galaxies at spatial resolutions of a few tens of parsecs. So far, adaptive optics systems are available mainly in near-infrared (near-IR) wavelengths, where the dust extinction at the central regions of galaxies is less important than at optical bands. In addition, strong absorption CO bands are present in the spectra of galaxies, originated in giant and supergiant stars that dominate the continuum emission in the central regions (e.g. Maraston 2005; Riffel et al. 2015b). Thus, near-IR IFS at 10-m telescopes provides a unique tool to map the stellar kinematics at central region of active galaxies, at unprecedented spatial resolution, by fitting the CO absorption band-heads (e.g. Riffel et al. 2015a).

In this paper, we map the stellar kinematics of the inner 3 arcsec  $\times$  3 arcsec of a sample of 16 nearby Seyfert galaxies. This work is part of a larger project in which our group *AGN Integral Field Spectroscopy* (AGNIFS) aims to study the feeding and feedback processes of a sample of 30 nearby Seyfert galaxies, selected by their X-ray luminosity. The kinematic maps presented here will be used to isolate gas non-circular motions in future works by our group and to quantify gas inflows and outflows.

This paper is organized as follows: Section 2 presents the sample and a description of the observations and data reduction procedure, while the spectral fitting procedure is presented in Section 3. The resulting stellar kinematics maps are presented and discussed in Section 4 and the kinematic derived parameters are compared with those characterizing the large-scale discs of the host galaxies in Section 5.1. Finally, Section 6 presents the main conclusions of this work.

## 2 SAMPLE AND OBSERVATIONS

### 2.1 The sample

Our sample comprises 16 AGN host galaxies: 8 from a large Gemini proposal (PI Storchi-Bergmann) to obtain Near-Infrared Integral Field Spectrograph (NIFS) observations of 20 AGNs selected from the *Swift*-BAT 60-month catalogue (Ajello et al. 2012) to have 14–195 keV luminosities  $L_X \geq 10^{41.5}$  erg s<sup>-1</sup>, and 8 from previous similar NIFS observations by our group of nearby AGN hosts. Four of these eight galaxies have similar  $L_X$  luminosities and four are not in the *Swift*-BAT catalogue. One additional source (Mrk 79) was observed in previous run with similar NIFS configuration, but the signal-to-noise ratio of the CO absorption band-heads was not high enough to allow stellar kinematics measurements. By the end of 2018, we should have additional observations of another 13 galaxies of the large proposal and thus will have in the end a total of 29 galaxies comprising 20 *Swift*-BAT selected galaxies plus the 8 galaxies included in this study (plus Mrk 79) that comprise what we call a ‘complementary sample’, and identified by the footnote *a* in Table 1.

Additional criteria for the sample is that the redshift is  $z \leq 0.015$ , and to be accessible for NIFS ( $-30^\circ < \delta < 73^\circ$ ). The  $L_X$  criterion above defining the sample of the large proposal was adopted because the *Swift*-BAT 14–195 keV band measures direct emission from the AGN rather than scattered or re-processed emission, and is much less sensitive to obscuration in the line of sight (LOS) than soft X-ray or optical wavelengths, allowing a selection based only on the AGN properties. To assure that we would be able to probe the feeding and feedback processes via the gas kinematics, we further selected the galaxies having previously observed extended gas emission (e.g. Schmitt & Kinney 2000) and [O III] $\lambda$ 5007 luminosities. We have excluded from the sample a few galaxies that had guiding problems in the observations. A complete characterization of the sample will be presented in a forthcoming paper (Riffel et al., in preparation).

So far, we have already observed 20 galaxies with NIFS, but only for 16 of them we were able to measure the stellar kinematics by



fitting the  $K$ -band CO absorption bands at  $2.3\ \mu\text{m}$ . We were not able to obtain reliable fits of the remaining four objects (Mrk 3, Mrk 79, NGC 4151 and NGC 1068) due to the dilution of the  $K$ -band CO band-heads due to strong continuum emission. For the latter two, the stellar kinematics has already been studied using the  $H$ -band spectra (Storchi-Bergmann et al. 2012; Onken et al. 2014). The 16 galaxies selected for this study are listed in Table 1, together with relevant information.

## 2.2 Observations

We used the Gemini NIFS (McGregor et al. 2003) to observe the galaxies listed in Table 1. All observations were obtained using the Gemini North Adaptive Optics system ALTAIR from 2008 to 2016. The observations followed the standard Object–Sky–Sky–Object dither sequence, with off-source sky positions since all targets are extended, and individual exposure times that varied according to the target. The ‘HK\_G0603’ filter and the ‘KL\_G5607’ and ‘K\_G5605’ gratings were used during the observations. Most of the observations were performed in the  $K_I$  band, with the spectra centred at  $2.3\ \mu\text{m}$ , while for five galaxies the spectra were obtained at the  $K$  band and centred at  $2.2\ \mu\text{m}$ . The spectral range for the  $K_I$  data is  $\sim 2.080\text{--}2.500\ \mu\text{m}$  and for the  $K$  band is  $\sim 1.980\text{--}2.400\ \mu\text{m}$ . Both ranges include the  $^{12}\text{CO}$  and  $^{13}\text{CO}$  absorption band-heads at  $\sim 2.3\ \mu\text{m}$  for all galaxies, used to measure the stellar kinematics.

The spectral resolution ranges between  $3.2$  and  $3.6\ \text{\AA}$ , as obtained from the measurement of the full width at half-maximum (FWHM) of ArXe lamp lines, used to wavelength calibrate the spectra, close to the central wavelength. This translates to resolutions in the range of  $42\text{--}47\ \text{km s}^{-1}$  in the velocity space. The angular resolution is in the range of  $0.12\text{--}0.20$  arcsec, derived from the FWHM of flux distribution of the standard stars, corresponding to few tens of parsecs at the distance of most galaxies. More details about the observations are shown in Table 1.

## 2.3 Data reduction

The data reduction followed the standard procedure and was accomplished by using tasks specifically developed for NIFS data reduction, contained in the NIFS package, which is part of GEMINI IRAF package, as well as generic IRAF tasks and IDL scripts. The data reduction procedure included the trimming of the images, flat-fielding, sky subtraction, wavelength and s-distortion calibrations. The telluric absorptions have been removed using observations of telluric standard stars with A spectral type. These stars were used to flux calibrate the spectra of the galaxies by interpolating a blackbody function to their spectra. Finally, data cubes were created for each individual exposure at an angular sampling of  $0.05\ \text{arcsec} \times 0.05\ \text{arcsec}$  and combined in a final data cube for each galaxy. All data cubes cover the inner  $\sim 3\ \text{arcsec} \times 3\ \text{arcsec}$ , with exception of the data cube for NGC 4051 that covers the inner  $\sim 3\ \text{arcsec} \times 4\ \text{arcsec}$ , via spatial dithering during the observations (Riffel et al. 2008).

The median value of the signal-to-noise ratio (S/N) in the continuum of our sample ranges from 10 to 30, with the maximum value of up to  $S/N \sim 100$  observed for the nuclear spectrum of NGC 4051. The median value of the S/N for the  $^{12}\text{CO}$  (2-0) band-head at  $2.29\ \mu\text{m}$  is larger than 3 for all galaxies of the sample.

Detailed descriptions of the observations and data reduction procedures for the galaxies already analysed are presented in Riffel, Storchi-Bergmann & Nagar (2010) for Mrk 1066, Riffel & Storchi-Bergmann (2011b) for Mrk 1157, Diniz et al. (2015) for NGC 2110 and Riffel et al. (2008) for NGC 4051. For the remaining objects, a

more detailed discussion will be presented in a forthcoming paper (Riffel et al., in preparation).

## 3 SPECTRAL FITTING

The stellar line-of-sight velocity distribution (LOSVD) of each galaxy was obtained by fitting the spectra within the spectral range of  $\sim 2.26\text{--}2.40\ \mu\text{m}$  (rest wavelengths), which includes the CO absorption band-heads from  $\sim 2.29$  to  $\sim 2.40\ \mu\text{m}$  (Winge et al. 2009), usually amongst of the strongest absorption lines in the central region of galaxies (e.g. Riffel, Rodríguez-Ardila & Pastoriza 2006; Riffel et al. 2015b). The used spectral range also includes weaker absorption lines from Mg I and Ca I at  $2.26\text{--}2.28\ \mu\text{m}$ . The spectra were fitted by using the penalized pixel-fitting PPF method (Cappellari & Emsellem 2004), which finds the best fit to a galaxy spectrum by convolving stellar spectra templates with a given LOSVD, under the assumption that it is reproduced by Gauss–Hermite series.

The PPF code requires the use of spectral templates that are used to reproduce the galaxy’s spectrum. We used the spectra of the Gemini library of late spectral type stars observed with the Gemini Near-Infrared Spectrograph (GNIRS) IFU and NIFS (Winge et al. 2009) as stellar templates. The spectral resolution of the stellar library is very similar to that of the spectra of the galaxies of our sample and the library includes stars with spectral types from F7 to M5, minimizing the template mismatch problem.

The spectral range used in the fit includes the [Ca VIII]  $\lambda 2.321\ \mu\text{m}$  emission line, which ‘contaminates’ the  $(3-1)^{12}\text{CO}$  band-head and affects the stellar kinematics measurements (Davies et al. 2006; Riffel et al. 2008). The [Ca VIII] is seen at the nucleus and close vicinity, being unresolved for most galaxies of our sample and we have excluded its spectral region from the fit when the line is present. In addition, we used the *clean* parameter of PPF to reject all spectral pixels deviating more than  $3\sigma$  from the best fit, to exclude possible remaining sky lines and spurious features.

In Fig. 1, we present examples of typical fits for the galaxies NGC 1052, NGC 788 and NGC 5899. The left-hand panels show the fits for the nuclear spectrum, while extra-nuclear spectra are shown at the right-hand panels, extracted at  $0.5\ \text{arcsec}$  south of the nucleus – chosen to represent typical extra-nuclear spectra. The observed spectra are shown as black dotted lines, the fits are shown in red and the regions masked during the fits, following the criteria explained above, are shown in green. As can be seen for NGC 788, the cleaning procedure properly excluded the region affected by the [Ca VIII]  $\lambda 2.321\ \mu\text{m}$  emission line, as well as spurious features. For all galaxies, the standard deviations of the residuals (observed – model) are similar to that of the galaxy spectra derived within a  $200\ \text{\AA}$  spectral window, bluewards to the first CO absorption band-head, meaning that the spectra are well reproduced by the models.

The PPF code returns as output, measurements for the radial velocity ( $V_{\text{LOS}}$ ), stellar velocity dispersion ( $\sigma$ ), and higher order Gauss–Hermite moments ( $h_3$  and  $h_4$ ) for each spatial position, as well as their associated uncertainties. Using the results of the fit, we have constructed two-dimensional maps for each fitted parameter ( $V_{\text{LOS}}$ ,  $\sigma$ ,  $h_3$  and  $h_4$ ), which are presented in the next section.

## 4 STELLAR KINEMATICS

Figs 2–12 show the resulting maps for the stellar kinematics of our sample. The stellar kinematics for NGC 4051, NGC 2110, NGC 5929, Mrk 1066 and Mrk 1157 was already discussed in previous works by our group (see references in Table 1). Thus, we present

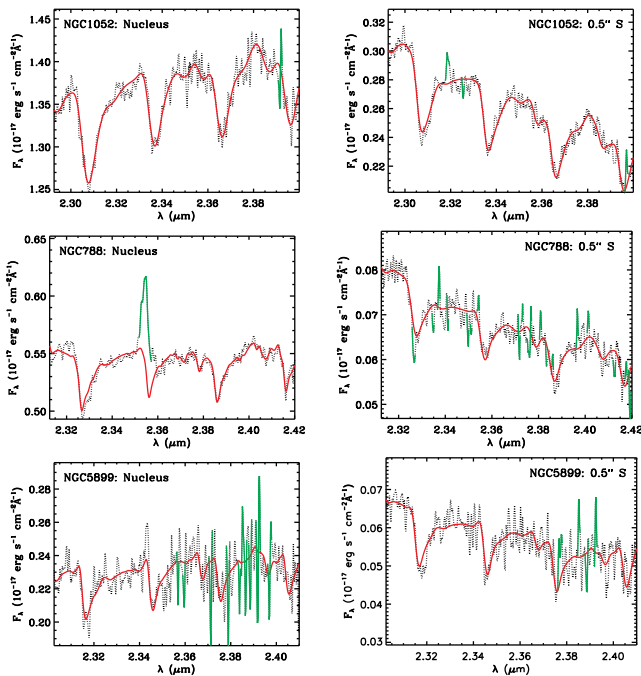


**Figure 1.** Examples of fits for the nuclear spectrum (left) and typical extra nuclear spectrum (right) for NGC 1052 (top panels), NGC 788 (centre panels) and NGC 5899 (bottom panels). The observed spectra are shown as black dotted lines, the best-fitting models as red continuous lines and the masked regions (following the criteria explained in the text) during the fits are shown in green.

the corresponding maps for these galaxies in Figs A1–A5 of the Appendix A, to be published online only.

To characterize the LOS velocity fields, we have symmetrized the stellar velocity field, using the *fit\_kinematic\_pa*<sup>1</sup> routine. This routine measures the global kinematic position angle (PA) and systemic velocity of the galaxy from integral field observations of the galaxy’s kinematics. The method is described in Krajnović et al. (2006). Cappellari et al. (2007) and Krajnović et al. (2011) show examples of application of the method to study the large-scale stellar kinematics of large sample of galaxies of the SAURON and ATLAS<sup>3D</sup> surveys.

In addition, we fitted the LOS velocity fields by a rotating disc model. The model was obtained using the DiskFit routine (Barnes & Sellwood 2003; Reese et al. 2007; Spekkens & Sellwood 2007; Sellwood & Sánchez 2010; Kuzio de Naray et al. 2012; Sellwood & Spekkens 2015) to fit the symmetrized velocity fields. This code fits non-parametric kinematic models to a given velocity field allowing the inclusion of circular and non-circular motions in a thin disc. Examples of application of this code for the gas and stellar kinematics of the inner region of active galaxies are shown in Fischer et al. (2015) and Riffel et al. (2015c), respectively. We fitted the symmetrized velocity field, instead of the observed one, as the rotating disc model is expected to be symmetric and small fluctuations in velocity due to higher uncertainties at some locations would result in a worse model for the stellar kinematics. During the fit, we have fixed the kinematical centre to the position of the peak of the continuum emission, and the systemic velocity and orientation

of the line of nodes of the galaxy were fixed as the values obtained from the symmetrization of the velocity field to reduce the number of parameters to be fitted. The ellipticity and disc inclination were allowed to vary during the fit and the resulting fitted values for each galaxy are shown in Table 2.

Figs 2–12 are organized as follows:

(i) Top-left panel: the K-band image, obtained as the average flux between 2.20 and 2.30  $\mu\text{m}$ . The continuous line shows the orientation of the kinematic major axis and the dotted line shows the orientation of the minor axis of the galaxy, obtained from the symmetrization of the stellar velocity field. The colour bar shows the flux scale in units of  $10^{-17} \text{ erg s}^{-1} \text{ cm}^{-2} \text{ \AA}^{-1}$ .

(ii) Top-centre panel: measured LOS stellar velocity field obtained from the fit of the spectra using the PPXF routine (Cappellari & Emsellem 2004), following the procedure described in Section 3.

(iii) Top-right panel: symmetrized velocity field. The colour bar is shown in units of  $\text{km s}^{-1}$  and the systemic velocity of the galaxy was subtracted.

(iv) Middle-left panel: rotating disc model, obtained by fitting the symmetrized velocity field.

(v) Middle-centre panel: residual map obtained by subtracting the rotating disc model from the observed velocity field.

(vi) Middle-right panel: residual map obtained by subtracting the rotating disc model from the symmetrized velocity field, constructed to verify if the velocity field is well reproduced by the model.

(vii) Bottom-left panel: stellar velocity dispersion ( $\sigma$ ) map. The colour bar shows the  $\sigma$  in  $\text{km s}^{-1}$  units.

(viii) Bottom-centre panel: map for the  $h_3$  Gauss–Hermite moment. The  $h_3$  moment measures asymmetric deviations of the LOSVD from a Gaussian velocity distribution (Gerhard 1993; van der Marel & Franx 1993; Riffel 2010). High (positive)  $h_3$  values correspond to the presence of red wings in the LOSVD, while low (negative)  $h_3$  values correspond to the presence of blue wings.

(ix) Bottom-right panel: map for the  $h_4$  Gauss–Hermite moment that measures symmetric deviations of the LOSVD relative to a Gaussian velocity distribution. High (positive)  $h_4$  values indicate LOSVD is more ‘pointy’ than a Gaussian, while low (negative)  $h_4$  values indicate profiles more ‘boxy’ than a Gaussian.

In all figures, north is up and east is to the left and the grey regions represent masked locations. In these regions, it was not possible to obtain good fits due to low signal-to-noise ratio of the spectra or due to the non-detection of absorption lines (e.g. due to the dilution of the absorption lines by strong AGN continuum emission). The masked regions correspond to locations where the uncertainty in velocity or velocity dispersion is higher than  $30 \text{ km s}^{-1}$ , while for most other locations the uncertainties are smaller than  $15 \text{ km s}^{-1}$ .

A rotating disc pattern is recognized in the LOS velocity field for all galaxies, with a straight zero velocity line for most of them. For two galaxies – Mrk 1066 (Riffel & Storchi-Bergmann 2011a) and NGC 5899 (Fig. 10) – an S-shape zero velocity line is observed, which is a signature of the presence of a nuclear bar or spiral arms in these galaxies (e.g. Combes et al. 1995; Emsellem et al. 2006). For most galaxies, the maximum amplitude of the rotation curve is expected to be observed outside of the NIFS field of view (FoV). The rotation disc signature is clearly seen in the one-dimensional plots shown in Fig. B1, obtained by averaging the velocity and  $\sigma$  values within a pseudo-slit with width of 0.25 arcsec oriented along the major axis of the galaxy. The

<sup>1</sup> This routine was developed by M. Cappellari and is available at <http://www-astro.physics.ox.ac.uk/mxc/software>.

**Table 2.** Kinematic parameters obtained by symmetrize the stellar velocity. Col. 1: galaxy name; cols 2 and 3: systemic velocity ( $V_s$ ) corrected for the heliocentric frame and orientation of the line of nodes ( $\Psi_0$ ) derived from the symmetrization of the velocity fields; cols 4 and 5: disc ellipticity ( $e$ ) and inclination ( $i$ ) derived by modelling the velocity field using the DiskFit routine; cols 6 and 8: orientation of the major axis, ellipticity and inclination of the large-scale disc, as available at NED; col 9: the nuclear stellar velocity dispersion measured within a circular aperture with 150 pc diameter.

Galaxy	FitKinematicPA		DiskFit		Large-scale disc			$\sigma$ (km s <sup>-1</sup> )
	$V_s$ (km s <sup>-1</sup> )	$\Psi_0$ (°)	$e$	$i$ (°)	$\Psi_{\text{NED}}$ (°)	$e_{\text{NED}}$	$i_{\text{NED}}$ (°)	
NGC788	4034	120 ± 3	0.07 ± 0.01	20.8 ± 0.2	100	0.67	42.3	187 ± 4
NGC1052	1442	114 ± 3	0.32 ± 0.01	47.5 ± 0.2	120	0.71	45.6	245 ± 4
NGC2110	2335	156 ± 3	0.26 ± 0.01	42.5 ± 0.3	160	0.63	38.7	238 ± 5
NGC3227	1174	156 ± 3	0.30 ± 0.01	45.4 ± 0.2	152	0.88	62.0	130 ± 7
NGC3516	2631	54 ± 3	0.05 ± 0.01	18.2 ± 0.8	7	0.69	43.9	186 ± 3
NGC4051	717	130 ± 9	0.20 ± 0.01	37.3 ± 0.9	142	0.84	56.6	72 ± 3
NGC4235	2276	54 ± 3	0.25 ± 0.01	41.2 ± 0.5	50	0.94	70.1	183 ± 12
NGC4388	2537	96 ± 3	0.11 ± 0.01	27.7 ± 0.3	89	0.95	71.3	106 ± 6
NGC5506	1878	96 ± 3	0.48 ± 0.01	58.7 ± 0.3	90	0.97	76.1	–
NGC5548	5128	108 ± 3	0.51 ± 0.04	60.9 ± 6.8	60	0.34	19.9	276 ± 22
NGC5899	2616	24 ± 3	0.54 ± 0.01	62.7 ± 0.3	25	0.92	67.7	147 ± 9
NGC5929	2491	30 ± 9	0.51 ± 0.01	60.7 ± 0.5	38	0.69	43.9	134 ± 5
MRK607	2781	138 ± 3	0.47 ± 0.01	58.2 ± 0.1	135	0.94	70.1	132 ± 4
MRK766	3855	66 ± 3	0.05 ± 0.02	18.2 ± 3.7	110	0.77	50.2	78 ± 6
MRK1066	3583	120 ± 3	0.36 ± 0.01	50.2 ± 0.3	140	0.92	66.4	103 ± 4
MRK1157	4483	114 ± 3	0.29 ± 0.01	45.1 ± 0.9	95	0.88	61.3	92 ± 4

deprojected velocity amplitude within the NIFS FoV ranges from  $\sim 50$  to  $\sim 300$  km s<sup>-1</sup>.

For five galaxies, the maximum  $\sigma$  value is smaller than 100 km s<sup>-1</sup>, seven have maximum  $\sigma$  in the range of 100–150 km s<sup>-1</sup> and four show the maximum  $\sigma > 150$  km s<sup>-1</sup>. In addition, distinct structures of low- $\sigma$  values ( $\sim 50$ – $80$  km s<sup>-1</sup>) are seen in the maps: low- $\sigma$  rings or partial rings are seen for Mrk 1066, Mrk 1157, NGC 5929 and NGC 788. These rings have been identified by visual inspection and are marked in the corresponding  $\sigma$  maps as green ellipses. In all cases, the size of the structures is larger than the spatial resolution and the  $\sigma$  decrease is larger than the velocity resolution of the data. These structures have been attributed to intermediate-age stellar populations (ages in the range of 100–700 Myr; e.g. Riffel et al. 2010, 2011), with origin in kinematically colder regions that still preserve the kinematics of the gas from which they have been formed. Patches of low- $\sigma$  are seen for Mrk 607, NGC 2110, NGC 3516, NGC 4051, NGC 4235 and NGC 5899, while three objects (NGC 1052, NGC 3227 and NGC 4388) show a centrally peaked  $\sigma$  distribution. These rings and partial rings are located at distances from the nucleus ranging between 150 and 250 pc. Nuclear  $\sigma$  values for each galaxy are presented in the last column of Table 2, obtained by fitting the nuclear spectrum integrated within a circular aperture with radius of 75 pc.

Most galaxies show low  $h_3$  values ( $-0.10 < h_3 < 0.10$ ), suggesting that their LOSVDs are well represented by a Gaussian velocity distribution. Exceptions are Mrk 607, Mrk1066 and NGC 4051 that show  $h_3$  values larger than 0.15. For eight galaxies (NGC 1052, NGC 2110, NGC 3227, NGC 3516, NGC 4051, NGC 5506, Mrk 607 and Mrk 1066), the  $h_3$  map is anticorrelated with the velocity field, with positive  $h_3$  values seen at locations where rotation velocities are observed in blueshifts and negative  $h_3$  values associated with regions where the rotation velocities are observed in redshifts. A similar trend (but not so clear) is observed for other four galaxies (NGC 4235, NGC 4388, NGC 5929 and Mrk 1157). In Fig. B2, we present plots of the LOS velocity versus  $h_3$  for all galaxies, which show this anticorrelation clearly. The anticorrelation seen between  $h_3$  and the LOS velocity can be interpreted as due to the contribu-

tion of stars rotating slower than those in the galaxy disc, probably due to motion in the galaxy bulge (e.g. Emsellem et al. 2006; Ricci, Steiner & Menezes 2016).

The  $h_4$  moment maps show small values at most locations for all galaxies, with  $-0.05 < h_4 < 0.05$ . For some galaxies, which present strong low- $\sigma$  structures (e.g. Mrk 1066, Mrk 607 and NGC 4051), higher positive  $h_4$  values are observed co-spatial with the low- $\sigma$  regions. This is also seen in the plots presented in Fig. B2, which show a trend of higher values of  $\sigma$  being observed in regions with negative  $h_4$  values, while small  $\sigma$  values being associated with positive  $h_4$  values. We interpret this correlation between low- $\sigma$  and high  $h_4$  values as an additional support to the presence of young/intermediate age stars at these locations, as more peaked velocity distributions are expected for young stars (as they are located in a thin disc structure).

The rotating disc models reproduce well the observed velocity fields for all galaxies, as seen in the residual velocity maps that show values smaller than 20 km s<sup>-1</sup> at most locations. Table 2 shows the model parameters for each galaxy. The systemic velocities from the table are relative to the heliocentric frame. The deprojected velocity amplitude of the galaxies of our sample ranges from  $\sim 60$  km s<sup>-1</sup> (for NGC 4051 – an Sc galaxy) to  $\sim 340$  km s<sup>-1</sup> (for NGC 3516 – an S0 galaxy).

## 5 DISCUSSIONS

### 5.1 Comparison between kinematic and large-scale disc parameters

Table 2 shows the parameters derived from the symmetrization (using the FitKinematicPA routine) and from the fit of the rotation disc model (using the DiskFit code) of the velocity fields. These parameters can be compared to those obtained for the large-scale discs. The PA of the major axis from NED<sup>2</sup> ( $\Psi_{\text{NED}}$ ), shown in

<sup>2</sup> NASA/IPAC Extragalactic Database available at <http://ned.ipac.caltech.edu/>.



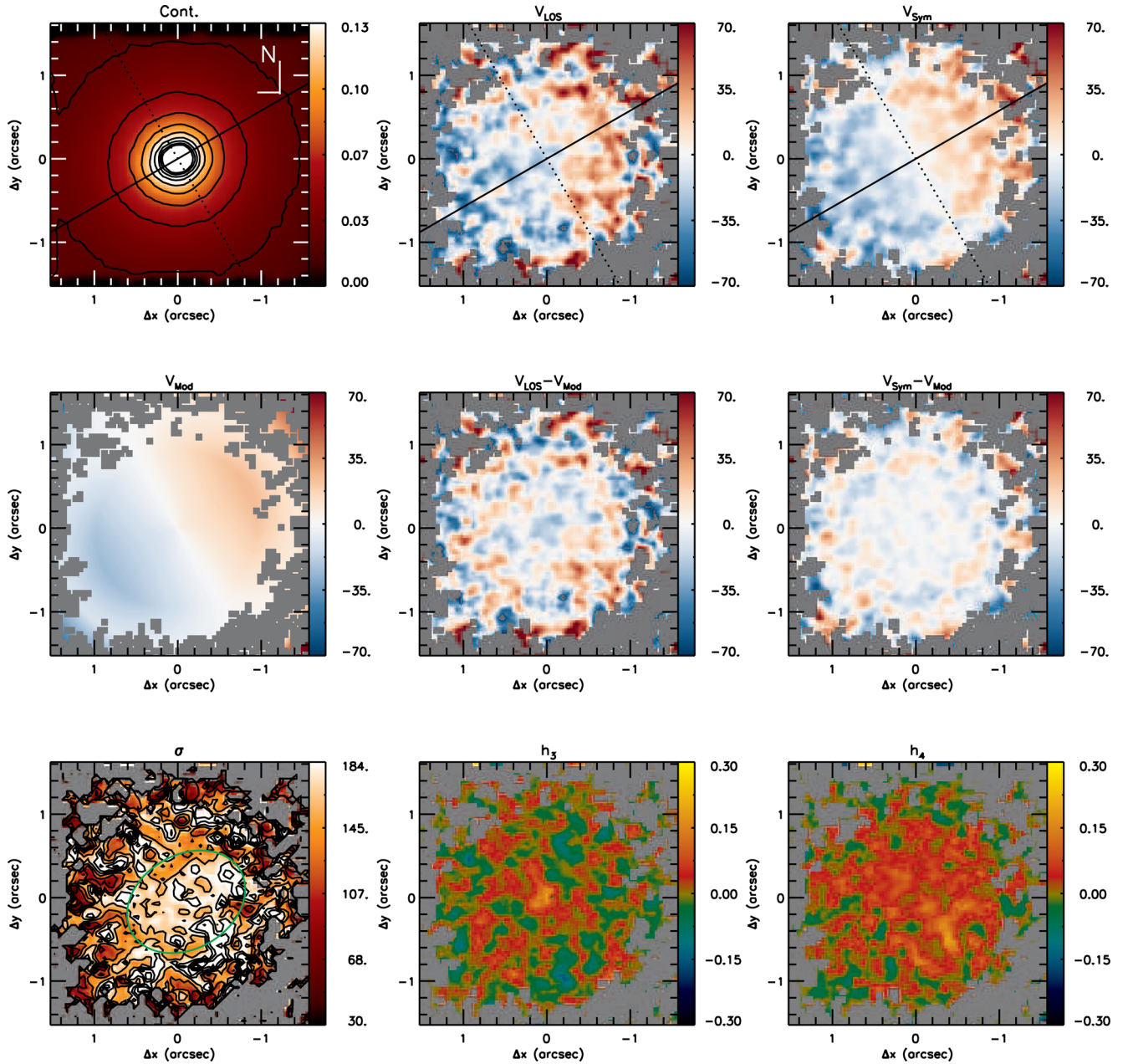


**Figure 2.** NGC 788: top-left: the  $K$ -band continuum image obtained by averaging the spectra, with the colour bar shown in units of  $10^{-17} \text{ erg s}^{-1} \text{ cm}^{-2} \text{ \AA}^{-1}$ ; top-middle: stellar velocity field; top-right: symmetrized velocity field; middle-left: rotating disc model; middle-middle: residual map for the symmetrized velocity field; middle-right: residual map for the observed velocity field; bottom-left: stellar velocity dispersion; bottom-middle:  $h_3$  Gauss–Hermite moment and bottom-right:  $h_4$  Gauss–Hermite moment. Grey regions are masked locations and correspond to regions where the signal to noise of the spectra was not high enough to get reliable fits. The continuous line identifies the orientation of the line of nodes and the dotted line marks the orientation of the minor axis of the galaxy. North is up and east left in all maps. The colour bar for velocity, model, residual maps and  $\sigma$  show the velocities in units of  $\text{km s}^{-1}$  and the systemic velocity of the galaxy was subtracted from the observed velocities.

Table 2 is derived from the  $K_S$  band photometry obtained from the Two Micron All Sky Survey (2MASS; Jarrett et al. 2003). The ellipticity ( $e_{\text{NED}}$ ) and inclination ( $i_{\text{NED}}$ ) of the disc are also obtained from the apparent major ( $a$ ) and minor ( $b$ ) axis available on NED data base from  $K_S$  images, as  $e_{\text{NED}} = 1 - \frac{b}{a}$  and  $i_{\text{NED}} = \arccos(b/a)$ , respectively.

In the left-hand panel of Fig. 13, we present a plot of the large-scale photometric PA of the major axis versus the kinematic PA derived from our NIFS velocity fields, constructed using the values of  $\Psi_0$  shown in Table 2. This plot shows that the small-scale

kinematic PA is in approximate agreement with the large-scale photometric one. The mean PA offset is  $\langle \Psi_0 - \Psi_{\text{NED}} \rangle = 3.9 \pm 5.7^\circ$ . Only for three galaxies (NGC 5548, Mrk 766 and NGC 3516), there are significant discrepancies between small-scale kinematic and large-scale photometric major axes. NGC 5548 and Mrk 766 are almost face-on galaxies and thus it is hard to obtain a precise determination of  $\Psi_0$ , both from photometry and kinematics, justifying the discrepancy. For NGC 3516, the  $\Psi_{\text{NED}}$  is distinct from that observed in optical images ( $\Psi_0 = 56^\circ$ ; Schmitt & Kinney 2000) and from the stellar kinematics based on optical IFS



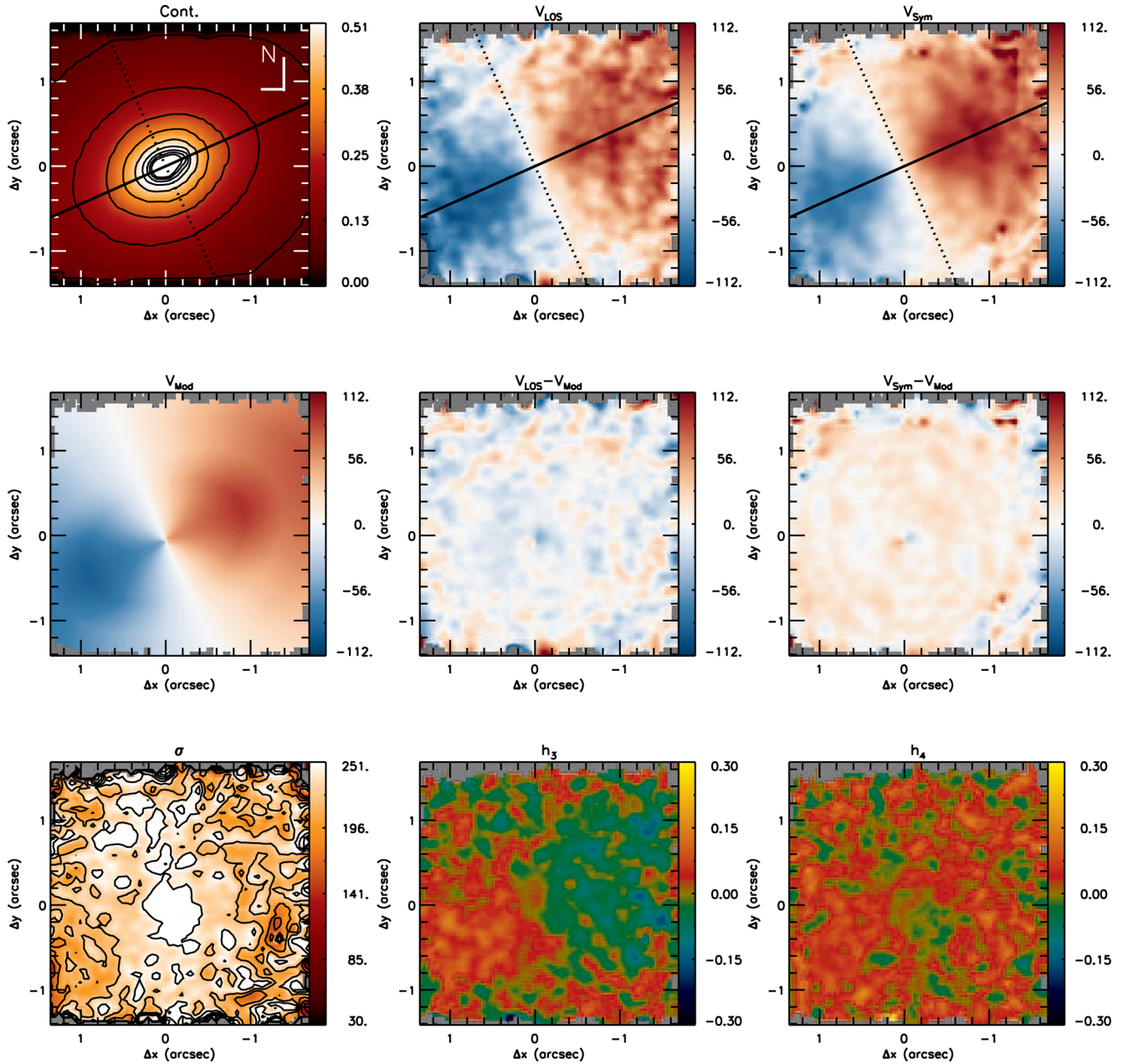


Figure 3. Same as Fig. 2 for NGC 1052.

( $\Psi_0 = 53^\circ$ ; Arribas et al. 1993). On the other hand, the  $\Psi_{\text{ONED}}$  for NGC 3516 is very similar to the orientation of the bar of the galaxy ( $\Psi_0 = -10^\circ$ ; Veilleux, Tully & Bland-Hawthorn 1993) and thus the value of  $\Psi_{\text{ONED}}$  may be biased due to the bar, which is stronger in near-IR bands.

Previous studies have found similar results. For example, the morphological study by Malkan, Gorjian & Tam (1998) of the inner kiloparsecs of nearby active galaxies showed that the resulting classification of the small-scale structure was very similar to the one given in the Third Reference Catalog (RC3; Corwin, Buta & de Vaucouleurs 1994), showing that not only the kinematic PA at small scale but also the photometric PA at small scale is similar to that at large scale.

Barbosa et al. (2006) used the Gemini Multi-Object Spectrograph (GMOS) IFU to map the stellar kinematics of the inner 200–900 pc

of six nearby active galaxies by fitting the stellar absorption lines of the Calcium triplet around 8500 Å and also found that the kinematic PA at small scale is in good agreement with the large-scale photometric measurements. Dumas et al. (2007) used optical IFS to map the stellar and gas kinematics of the central kiloparsec of a matched sample of nearby Seyfert and inactive galaxies at angular resolutions ranging from 0.9 to 2.5 arcsec, using the SAURON IFU on the *William Herschel Telescope*. They found that the orientations of the kinematic line of nodes are very similar with those derived from large-scale photometry for both active and inactive galaxies. Falcón-Barroso et al. (2006) present the stellar kinematics of a sample of 24 spiral galaxies using the SAURON IFU. Their sample includes only five active nuclei and they found misaligned photometric and kinematic axes for nine objects in their sample (only one being an active galaxy), interpreted as being due to

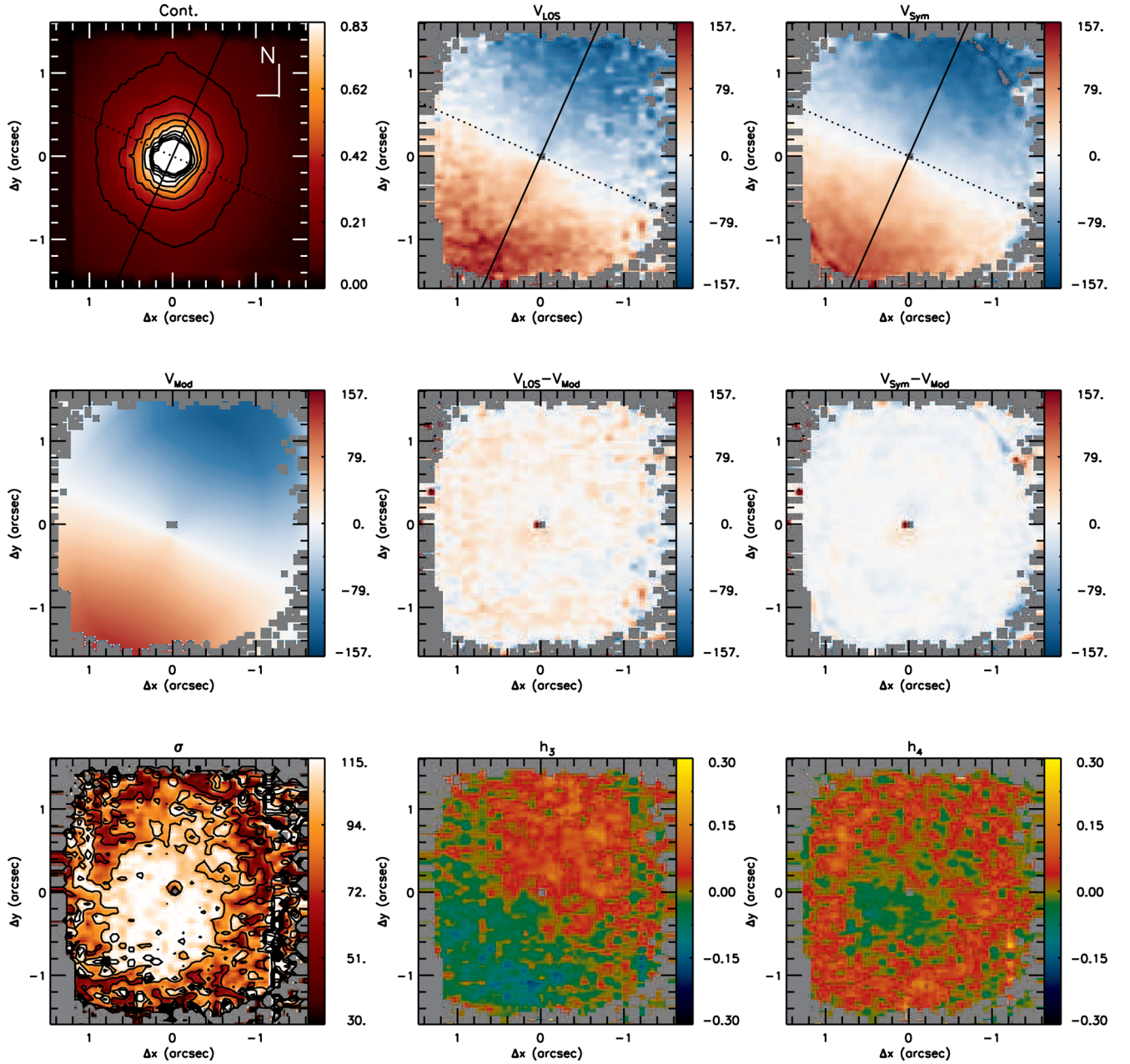


Figure 4. Same as Fig. 2 for NGC 3227.

non-axisymmetric structures (as bars) and more easily detected at low galaxy inclinations.

The middle and right-hand panels of Fig. 13 show the comparison between the large photometric ( $y$ -axis) and small kinematic ( $x$ -axis) scale disc inclination and ellipticity, respectively. In contrast to the orientation of the major axis of the galaxy, these parameters do not follow the same distribution at small and large scale. For most cases, both the inclination and the ellipticity of the disc at large scale are larger than that derived for the inner  $3 \text{ arcsec} \times 3 \text{ arcsec}$ . This result can be interpreted as being due to the fact that the large-scale measurements are dominated by the disc component as they are estimated from the apparent major and minor axis measurements obtained from large-scale  $K_S$  images, while at small scale, the near-IR emission is dominated by emission from evolved red stars at the bulge of the galaxy (e.g. Maraston 2005; Riffel et al. 2015b), which

play an important role in the observed morphology and kinematics observed with NIFS.

## 5.2 Gravitational potentials and comparison with previous studies

The velocity residual maps for all galaxies of our sample show small values, indicating that the stellar velocity fields are well reproduced by the rotating disc model, with kinematic axes that follow the same orientation of large-scale measurements. In addition, the de-projected rotation velocity amplitude is always larger than the mean velocity dispersion, indicating the stellar kinematics of the galaxies of our sample are dominated by regular rotation. We can compare our results with previous studies of the stellar kinematics of active and inactive galaxies.



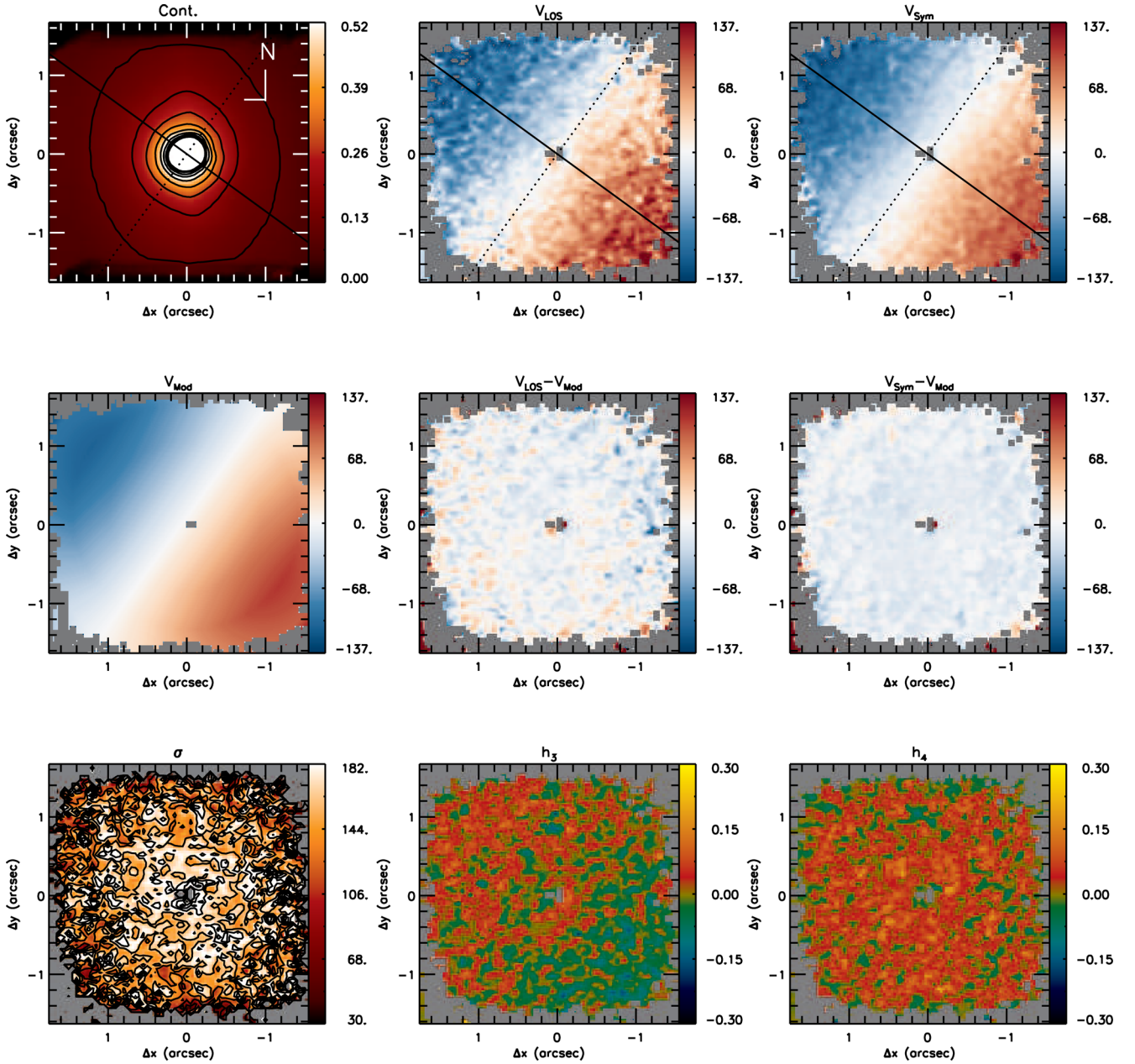


Figure 5. Same as Fig. 2 for NGC 3516.

Dumas et al. (2007) present the stellar kinematics of a sample of 39 active galaxies and a matched control sample, selected to have similar blue magnitudes, Hubble type and inclinations. They found that the stellar kinematics of both active and inactive galaxies show regular rotation patterns typical of disc-like systems. A similar result was found by Barbosa et al. (2006) using higher angular resolution ( $<1.0$  arcsec) IFS with Gemini Telescopes of a sample of six nearby Seyfert galaxies. In addition, they found partial rings of low- $\sigma$  values at 200–400 pc from the nucleus for three galaxies, interpreted as tracers of recently formed stars that partially keep the cold kinematics of the original gas from which they have formed. Falcón-Barroso et al. (2006) present kinematic maps for a sample of nearby spiral galaxies obtained with the SAURON IFU, which show regular stellar rotation for most galaxies. However, kinematic decoupled components are frequently seen in the inner region, as

sudden changes in the velocity field, which are often associated with a drop in the  $\sigma$  and anticorrelated  $h_3$  values with respect to the  $V_{LOS}$ . In addition, they found kinematic signatures of non-axisymmetric structures for 37 per cent of the galaxies of their sample (only one harbouring an AGN). For 20 per cent of their sample (five galaxies, none of them harbouring an AGN) they found kinematic signatures of bars as predicted in  $N$ -body simulations of barred potentials (e.g. Kuijken & Merrifield 1995; Bureau & Athanassoula 2005).

*Hubble Space Telescope (HST) H-band* images up to 10 arcsec radius and ground-based near-IR and optical images of a matched Seyfert versus non-Seyfert galaxy sample of 112 nearby galaxies show a statistically significant excess of bars amongst the Seyfert galaxies at practically all length-scales (Laine et al. 2002). In addition, they also found that Seyfert galaxies always show a preponderance of ‘thick’ bars compared to the bars in non-Seyfert

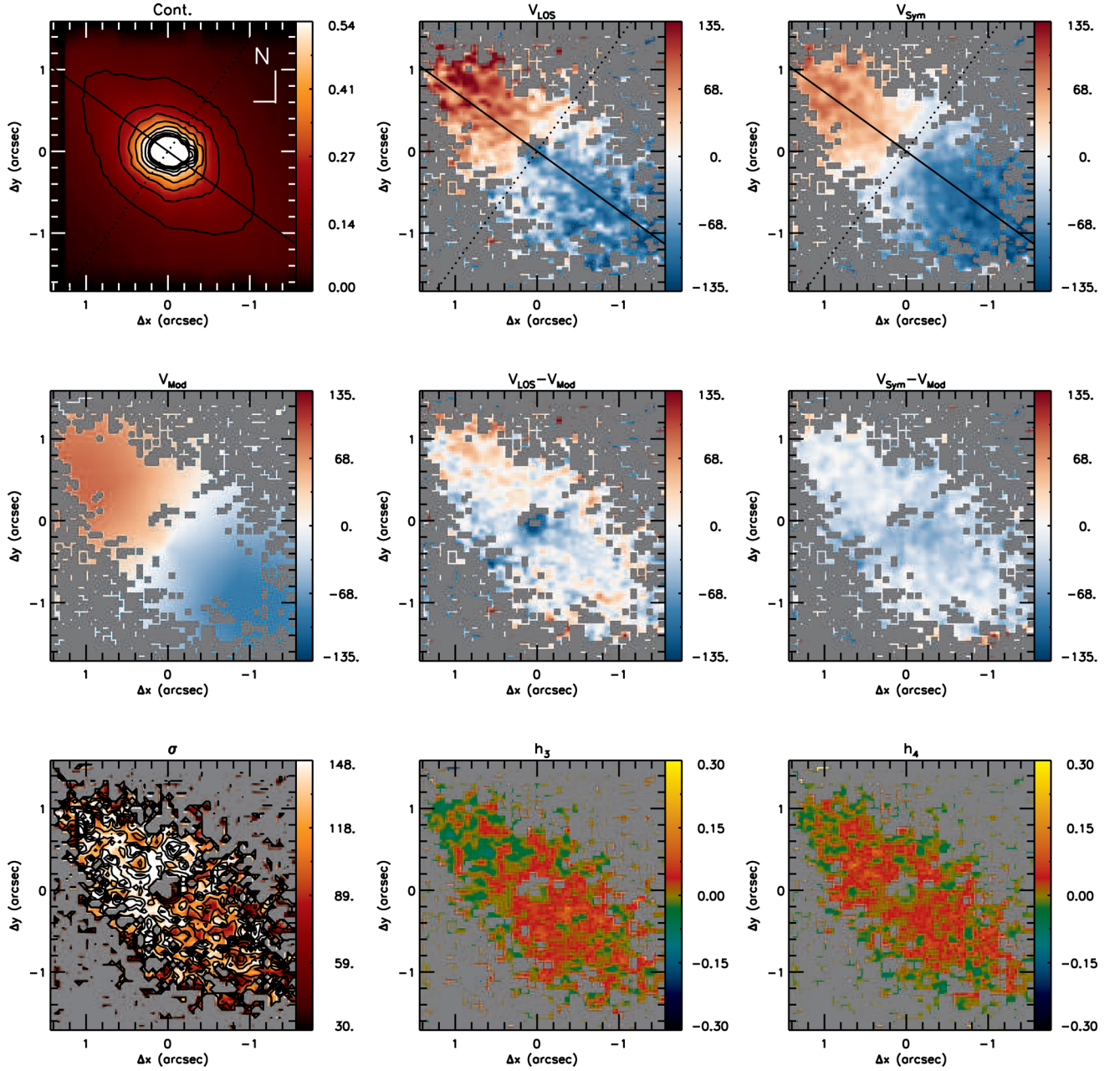


Figure 6. Same as Fig. 2 for NGC 4235.

galaxies. On the other hand, recent results show that AGN hosts at  $0.2 < z < 1.0$  show no statistically significant enhancement in bar fraction compared to inactive galaxies (e.g. Cheung et al. 2015). Large-scale bars are seen for 28.5 per cent of face-on spiral hosts of AGN, as obtained from the study of more than 6,000 AGN hosts from the Sloan Digital Sky Survey (SDSS; Alonso, Coldwell & Lambas 2013).

Our kinematic maps suggest the presence of nuclear bars in only two galaxies: Mrk 1066 and NGC 5899, as revealed by the presence of an S-shape zero velocity line observed in the  $V_{\text{LOS}}$  maps (e.g. Combes et al. 1995; Emsellem et al. 2006). This corresponds to only 12.5 per cent of our sample, although the statistics is low so far and this result is preliminary. The rest of the galaxies are dominated by rotation. The difference in the proportion of barred galaxies or non-axisymmetric structures in our study relative to that

of Falcón-Barroso et al. (2006) may be due to the small number of objects in both studies, and to the difference in the FoV of the two studies. Our FoV ( $3 \text{ arcsec} \times 3 \text{ arcsec}$ ) is smaller than those of previous studies, making it more difficult to identify kinematic signatures of bars as predicted in  $N$ -body simulations (e.g. Bureau & Athanassoula 2005), as double-hump rotation curves, broad  $\sigma$  profiles with a plateau at moderate radii and  $h_3 - V_{\text{LOS}}$  correlation over the projected bar length. On the other hand, the photometric detection of bars mentioned above are mainly obtained using large-scale images. Thus, our results suggest that the motion of the stars is dominated by the gravitational potential of the bulge, as the FoV of our observations is smaller than the bulge length for all galaxies.

To further investigate how the galactic potentials and deviations from ordered rotation are related to the host galaxy and AGN, we plotted the mean value of the modulus of the residual velocities



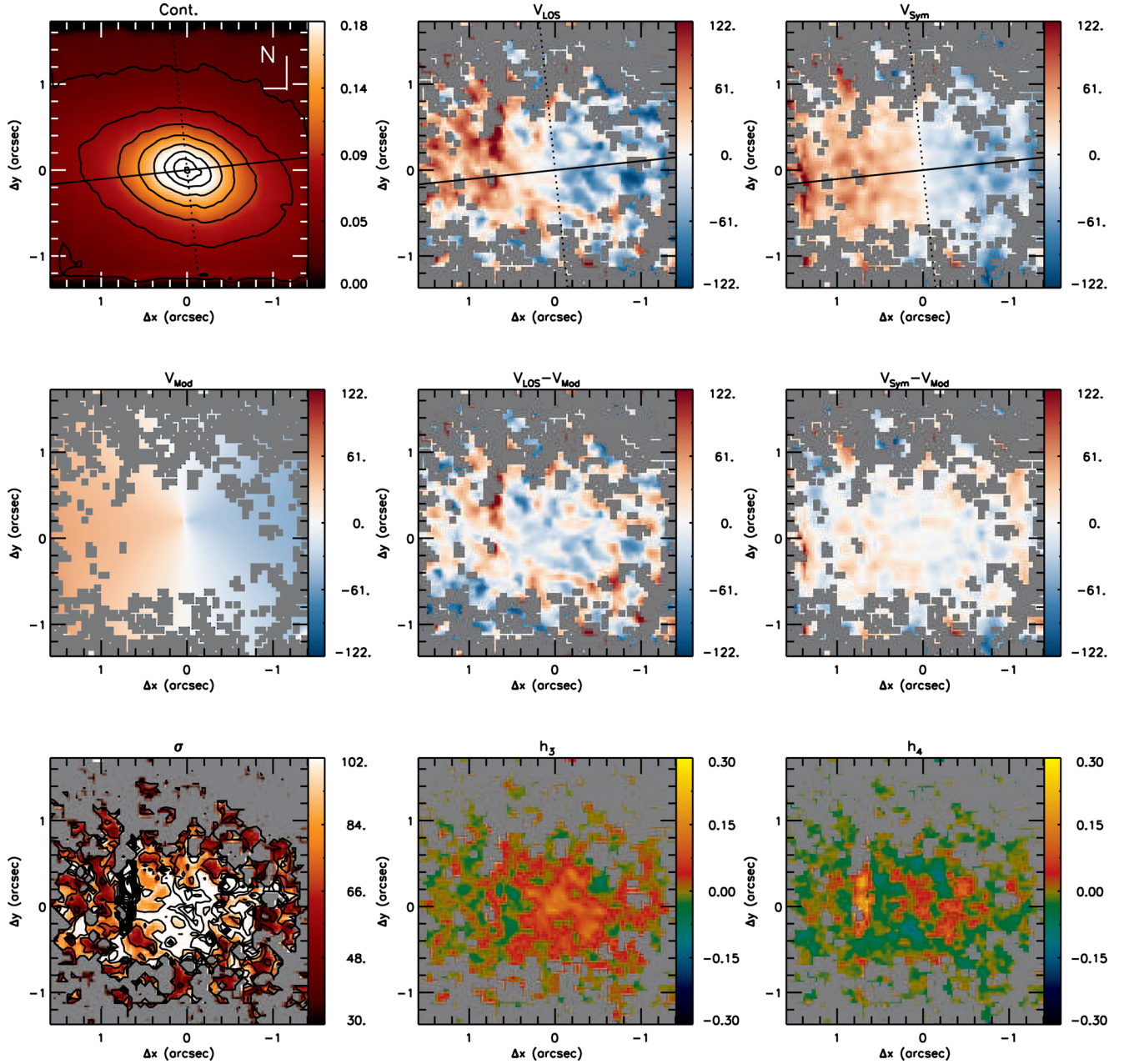


Figure 7. Same as Fig. 2 for NGC 4388.

( $|V_{\text{res}}|$ ), where  $V_{\text{res}} = V_{\text{LOS}} - V_{\text{mod}}$ , against the Hubble index and hard X-ray (14–195 keV) luminosity ( $L_X$ ) from the *Swift*-BAT 60-month catalogue (Ajello et al. 2012), which measures direct emission from the AGN. These plots are shown in Fig. 14. For four galaxies of our sample (MRK1066, MRK1157, MRK607 and NGC5929), there are no X-ray luminosities available in the BAT catalogue and thus the  $\langle |V_{\text{res}}| \rangle$  versus plot contains only 12 points. The  $\langle |V_{\text{res}}| \rangle$  was estimated as the mean value of 10,000 bootstrap realizations in which for each interaction the  $|V_{\text{res}}|$  is calculated for a sample selected randomly amongst the values observed in the residual map. The standard deviation in the simulated  $|V_{\text{res}}|$  represents the intrinsic scatter of each residual map and is used as the uncertainty for  $\langle |V_{\text{res}}| \rangle$ .

The top panel of Fig. 14 shows that there is no correlation between  $\langle |V_{\text{res}}| \rangle$  and Hubble index, with a Pearson correlation coefficient of

only  $R = 0.12$ . This result shows that large-scale structures do not affect significantly the stellar kinematics of the inner kiloparsec of the galaxies of our sample.

On the other hand, the bottom panel of Fig. 14 suggests that  $\langle |V_{\text{res}}| \rangle$  is correlated with  $L_X$ . We computed a Pearson correlation coefficient of  $R = 0.74$ , with less than 1 per cent of probability that this distribution of points can be generated by a random distribution. Although the number of points is small, this trend may mean that more luminous AGNs have a larger impact in the surrounding stellar dynamics. As a speculation, we propose that strong AGN may quench circum-nuclear star formation in the galaxy disc and thus the stellar motions have a more important component of bulge star kinematics. On the other hand, for lower luminosity AGNs, the active nuclei may not be powerful enough to quench the star formation and thus the stellar dynamics has a stronger

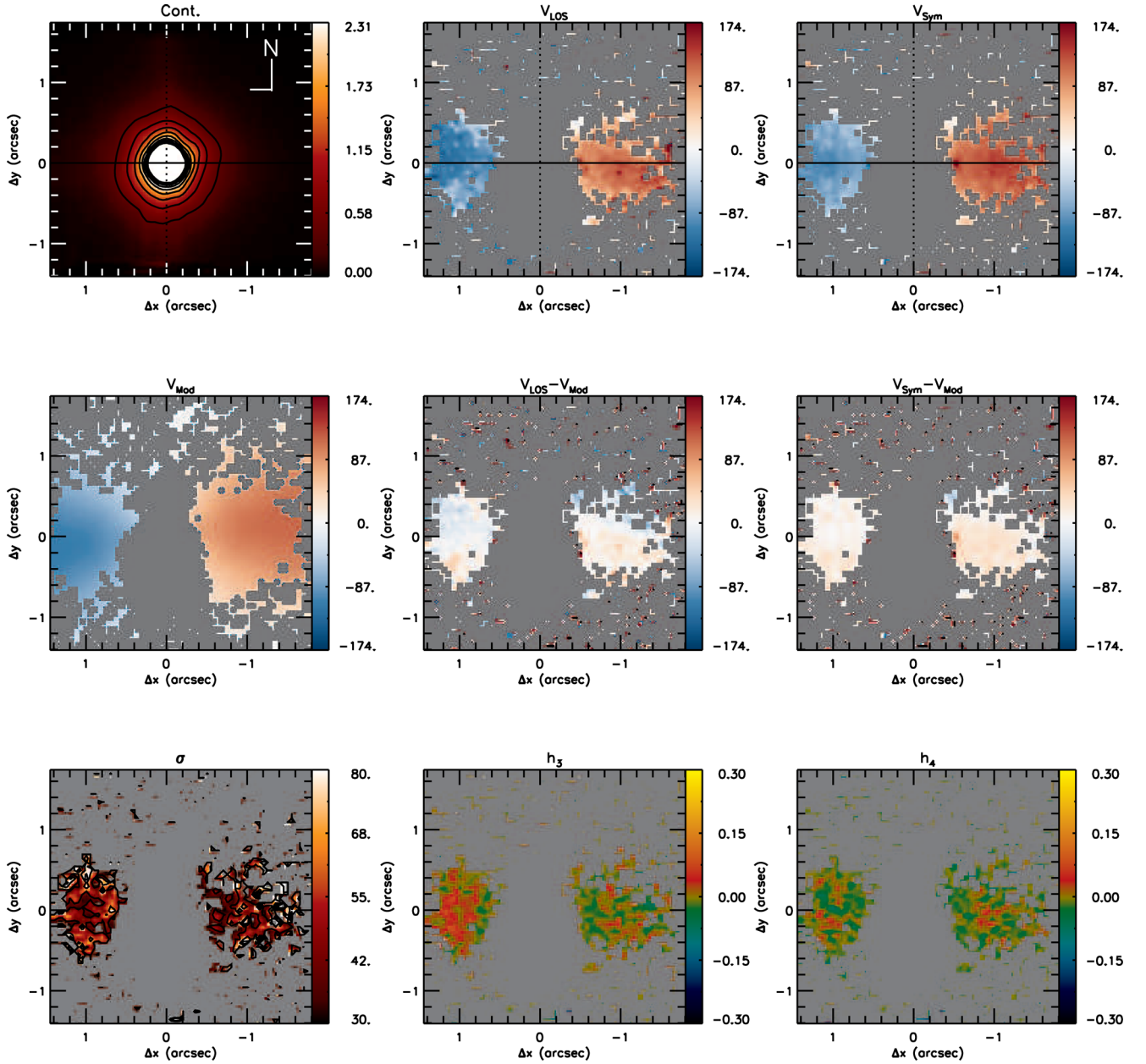


Figure 8. Same as Fig. 2 for NGC 5506.

contribution from stars more recently formed in the plane of the galaxy.

### 5.3 Implications to AGN feeding and star formation

The velocity dispersion maps show structures of lower  $\sigma$  than the surroundings ( $\sim 50\text{--}80\text{ km s}^{-1}$ ) for 10 galaxies (62 per cent) of our sample. Such velocity dispersion drops are commonly reported in the literature (e.g. Bottema 1989, 1993; Fisher 1997; García-Lorenzo, Mediavilla & Arribas 1999; Emsellem et al. 2001; Márquez et al. 2003; Barbosa et al. 2006; Falcón-Barroso et al. 2006) and have been interpreted as being tracers of relatively recent star formation as compared to the bulge stellar population (e.g. Emsellem et al. 2001, 2006; Márquez et al. 2003; Barbosa et al. 2006; Riffel et al. 2008). Indeed, stellar population synthesis using near-IR IFS with NIFS reveal that the low- $\sigma$  rings seen in Mrk1066 and

Mrk1157 are associated with an intermediate-age stellar population ( $< 700\text{ Myr}$ ; Riffel et al. 2010, 2011).

The low- $\sigma$  structures may be related to accretion of gas to the inner kiloparsec of galaxies as a result of streaming motions towards the nucleus along nuclear bars or dust spirals, observed for several active galaxies by our group (e.g. Fathi et al. 2006; Riffel et al. 2008; Storch-Bergmann et al. 2009; Riffel et al. 2013; Schnorr-Müller et al. 2014, 2016, 2017; Diniz et al. 2015; Lena et al. 2015) and other groups (e.g. Sánchez et al. 2009; van de Ven & Fathi 2010; Smajić et al. 2015). Several works have been aimed to investigate the presence of nuclear bars and dust spirals in active and inactive galaxies using high-resolution *HST* images (Laine et al. 2002; Pogge & Martini 2002; Simões Lopes et al. 2007; Martini, Dicken & Storch-Bergmann 2013). These studies reveal an excess of bars in Seyfert galaxies, when compared to a matched sample of inactive galaxies (Laine et al. 2002) and dust structures seem to be present in



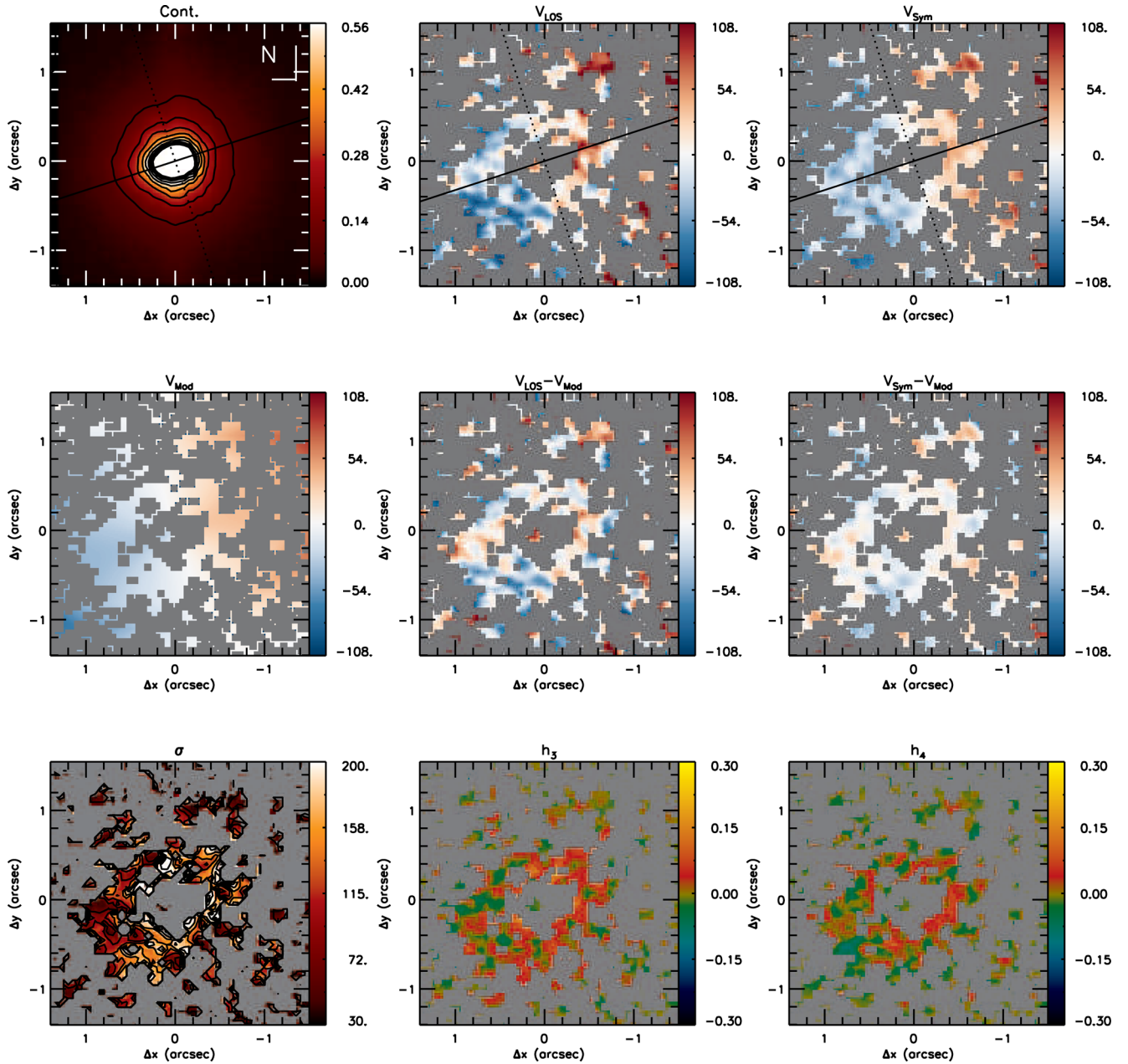


Figure 9. Same as Fig. 2 for NGC 5548.

all early-type AGN hosts, while only 26 per cent of inactive early-type show significant dust in the nuclear region (Simões Lopes et al. 2007). For late-type galaxies, large amount of dust is observed for both active and inactive galaxies (Simões Lopes et al. 2007).

The observed gas inflows mentioned above can lead to the accumulation of large reservoirs of gas that can feed both star formation and the AGN. In such scenario, it would be expected that low- $\sigma$  structures should be more frequent in active than in inactive galaxies. However, several studies report the presence of low- $\sigma$  structures in inactive galaxies. For example, Falcón-Barroso et al. (2006) found that at least 46 per cent of their sample of spiral galaxies show  $\sigma$ -drops, most of them being inactive. A similar result is reported by Ganda et al. (2006), who found central  $\sigma$  drops for many objects of their sample of 18 spiral galaxies. On the other hand, these drops are not commonly observed in elliptical galaxies

(Emsellem et al. 2004). Thus, the presence of low- $\sigma$  may be related to recent star formation in the inner kiloparsec of the galaxies of our sample, but possibly unrelated to the nuclear activity.

#### 5.4 The stellar kinematics and AGN feeding and feedback processes

This paper is the first of a series in which we will investigate the AGN feeding and feedback processes using *J* and *K* band NIFS observations of a sample of nearby active galaxies selected using the hard X-ray luminosity as main criterion. The results presented here will be used to compare gas and stellar kinematics to isolate non-circular motions, by constructing residual maps between the observed velocity fields for the ionized (traced by [Fe II] and H recombination lines) and molecular (traced by H<sub>2</sub> emission lines)

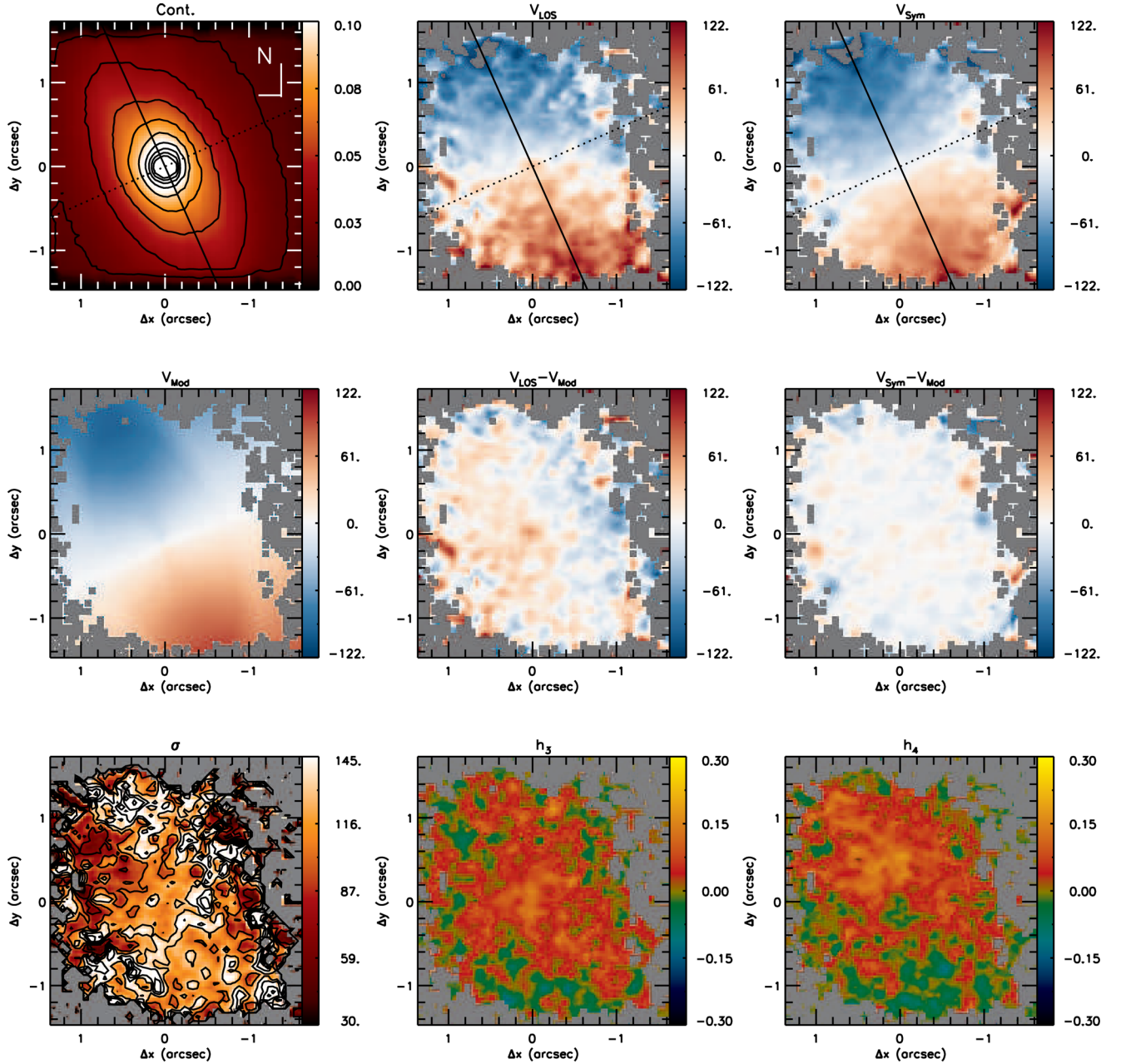


Figure 10. Same as Fig. 2 for NGC 5899.

gas and the rotating disc models presented here. The analysis of the residual maps, together with velocity channel maps along the emission-line profiles, will allow us to identify possible gas inflows and outflows. Similar methodology has already been successfully used by our AGNIFS group (e.g. Riffel et al. 2008; Riffel & Storchi-Bergmann 2011a; Riffel et al. 2013; Riffel & Storchi-Bergmann 2011b; Diniz et al. 2015). The gas inflow and outflow rates can be compared with AGN properties (e.g. bolometric luminosity and accretion rate) to draw a picture of the feeding and feedback processes in AGNs.

## 6 CONCLUSIONS

We used near-IR IFS to map the stellar kinematics of the inner  $3 \text{ arcsec} \times 3 \text{ arcsec}$  of a sample of 16 nearby Seyfert galaxies. We

present maps for the radial velocity, velocity dispersion and higher order Gauss–Hermite moments, obtained by fitting the CO stellar absorptions in the  $K$  band. The observed velocity fields were symmetrized and modelled by a thin rotating disc to derive kinematical parameters. The main results of this work are as following:

- (i) The observed velocity fields for all galaxies show regular rotation. In addition, for two galaxies (Mrk 1066 and NGC 5899) the velocity field shows an S-shape zero velocity line that is interpreted as a signature of nuclear bars.
- (ii) The residuals of the modelling of the stellar velocity field are correlated with the hard X-ray luminosity, suggesting that the nuclear source plays a role on the observed stellar dynamics of the inner kiloparsec of the galaxies, with stronger AGNs showing less-ordered stellar orbits than weak AGNs.



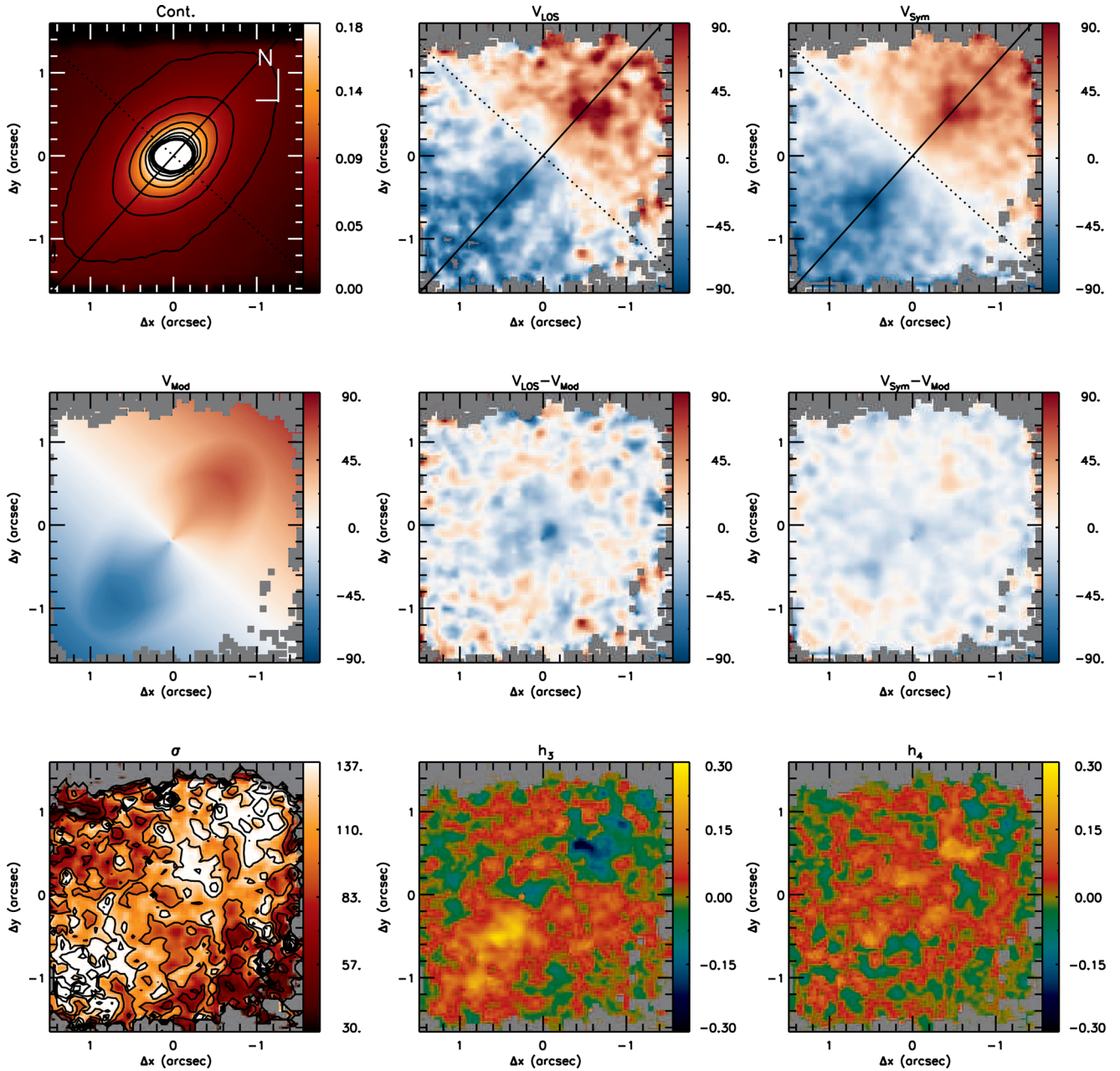


Figure 11. Same as Fig. 2 for Mrk 607.

(iii) The velocity dispersion maps show low- $\sigma$  ( $\sim 50\text{--}80\text{ km s}^{-1}$ ) rings for four galaxies (Mrk 1066, Mrk 1157, NGC 5929 and NGC 788) or ‘patches’ of low- $\sigma$  structures (for Mrk 607, NGC 2110, NGC 3516, NGC 4051, NGC 4235 and NGC 5899) at typical distances of 200 pc, interpreted as being originated in young/intermediate age stellar populations. Centrally peaked  $\sigma$  maps are observed for three galaxies (NGC 1052, NGC 3227 and NGC 4388).

(iv) The  $h_3$  moment is anticorrelated with the velocity field for eight galaxies (NGC 1052, NGC 2110, NGC 3227, NGC 3516, NGC 4051, NGC 5506, Mrk 607 and Mrk 1066) – positive  $h_3$  values seen at locations where the velocity field shows blueshifts and  $h_3 < 0$  for locations where the velocity field shows redshifts. The presence of these wings are attributed to the contribution of stars from the galaxy bulge that present lower rotation velocities.

(v) The  $h_4$  maps show small values at most locations for all galaxies. For the galaxies with low- $\sigma$  rings, higher  $h_4$  values are observed co-spatially with the ring, being interpreted as an additional signature of young/intermediate age stars at these locations.

(vi) The observed velocity fields are well reproduced by a rotating disc model, with deprojected velocity amplitudes in the range of  $\sim 60\text{--}340\text{ km s}^{-1}$ .

(vii) The orientations of the line of nodes derived from the small-scale velocity fields are similar to the photometric major axis orientations of the large-scale discs, while the disc ellipticity and inclination are smaller at small scale, as compared to those at large scale.

The stellar kinematics and rotating disc models derived in this work will be compared to the gas kinematics and flux distributions

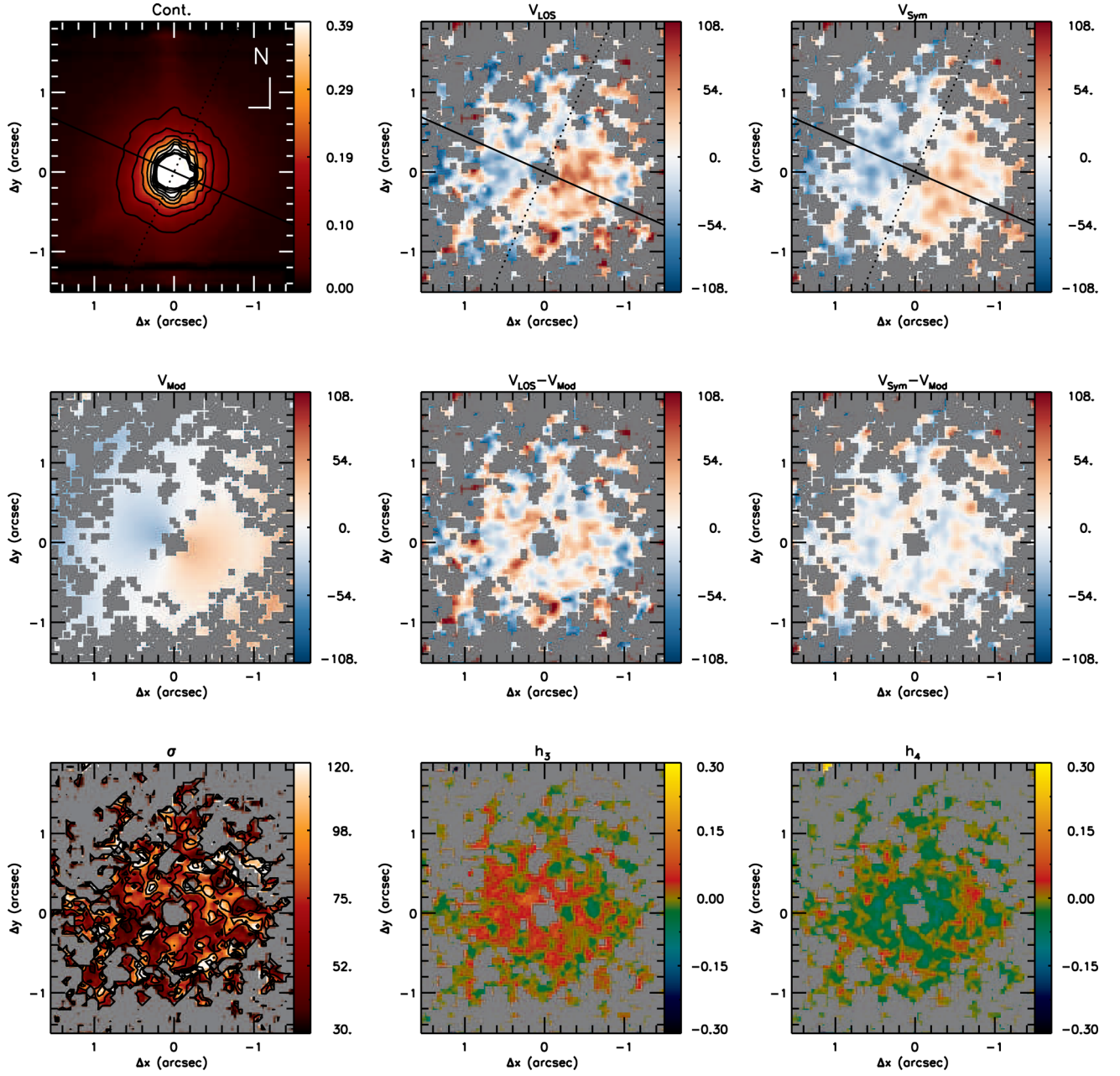


Figure 12. Same as Fig. 2 for Mrk 766.

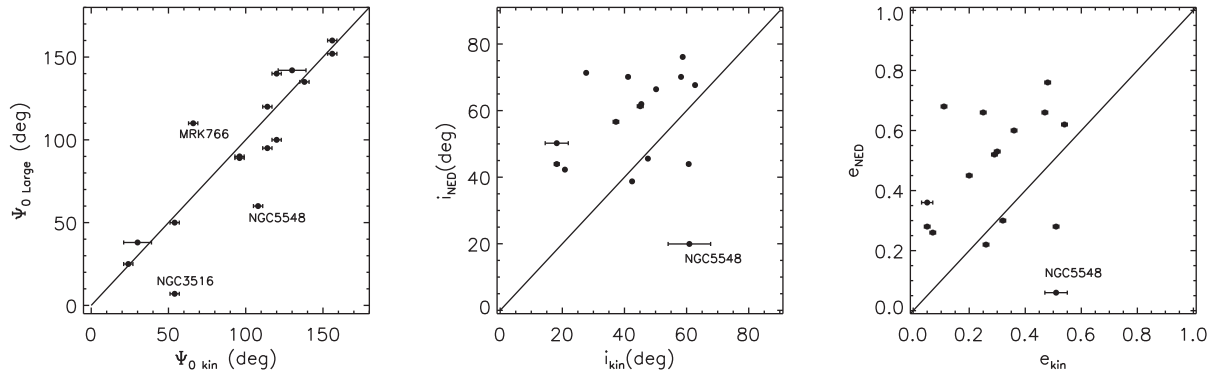
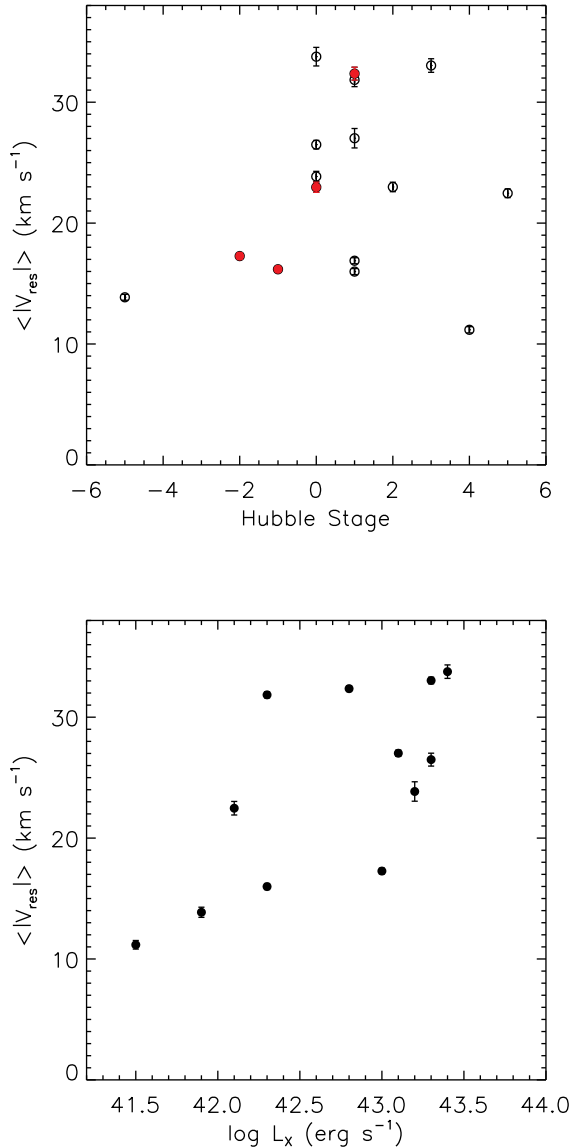


Figure 13. Comparison of large-scale photometric (y-axis) and small-scale kinematic (x-axis) PAs (left), inclination (middle) and ellipticity (right). Continuous lines show one-to-one relations.



**Figure 14.** Plots of the standard deviation of the residual maps ( $\langle |V_{\text{res}}| \rangle$ ) versus Hubble index (top) and X-ray luminosity ( $L_X$ , bottom). In the top panel, filled circles correspond to barred galaxies.

in future studies with the aim of isolating and quantifying non-circular motions in the gas of the galaxies of our sample to map and quantify feeding and feedback processes in our AGN sample.

## ACKNOWLEDGEMENTS

We thank an anonymous referee for useful suggestions that helped to improve the paper. This study is based on observations obtained at the Gemini Observatory, which is operated by the Association of Universities for Research in Astronomy, Inc., under a cooperative agreement with the NSF on behalf of the Gemini partnership: the National Science Foundation (United States), the Science and Technology Facilities Council (United Kingdom), the National Research Council (Canada), CONICYT (Chile), the Australian Research Council (Australia), Ministério da Ciência e Tecnologia (Brazil) and south-east CYT (Argentina).

This research has made use of the NASA/IPAC Extragalactic Database (NED) that is operated by the Jet Propulsion Laboratory,

California Institute of Technology, under contract with the National Aeronautics and Space Administration. We acknowledge the usage of the HyperLeda data base (<http://leda.univ-lyon1.fr>). RAR and RR thank CNPq and FAPERGS for financial support.

## REFERENCES

- Ajello M., Alexander D. M., Greiner J., Madejski G. M., Gehrels N., Burlon D., 2012, *ApJ*, 749, 21
- Alonso M. S., Coldwell G., Lambas D. G., 2013, *A&A*, 549, A141
- Arribas S., Mediavilla E., García-Lorenzo B., Del Burgo C., 1997, *ApJ*, 490, 227
- Barbosa F. K. B., Storchi-Bergmann T., Cid Fernandes R., Winge C., Schmitt H., 2006, *MNRAS*, 371, 170
- Barbosa F. K. B., Storchi-Bergmann T., Cid Fernandes R., Winge C., Schmitt H., 2009, *MNRAS*, 396, 2
- Barbosa F. K., Storchi-Bergmann T., McGregor P., Vale T. B., Riffel R. A., 2014, *MNRAS*, 455, 2353
- Barnes E. I., Sellwood J. A., 2003, *AJ*, 125, 1164
- Bottema R., 1989, *A&A*, 221, 236
- Bottema R., 1993, *A&A*, 275, 16
- Bureau M., Athanassoula E., 2005, *ApJ*, 626, 159
- Cappellari M., Emsellem E., 2004, *PASP*, 116, 138
- Cappellari M. et al., 2007, *MNRAS*, 379, 418
- Cheung E. et al., 2015, *MNRAS*, 447, 506
- Ciotti L. et al., 2010, *ApJ*, 717, 707
- Combes F., Boissé P., Mazure A., Blanchard A., 1995, *Galaxies and Cosmology*. Springer, Berlin
- Corwin H. G., Buta R. J., de Vaucouleurs G., 1994, *AJ*, 108, 2128
- Davies R. I. et al., 2006, *AJ*, 646, 754
- Diniz M. R., Riffel R. A., Storchi-Bergmann T., Winge C., 2015, *MNRAS*, 453, 1727
- Dumas G., Mundell C. G., Emsellem E., Nagar N. M., 2007, *MNRAS*, 379, 1249
- Elvis M., 2000, *ApJ*, 545, 63
- Emsellem E., Greusard D., Combes F., Friedli D., Leon S., Pécontal E., Wozniak H., 2001, *A&A*, 368, 52
- Emsellem E. et al., 2004, *MNRAS*, 352, 721
- Emsellem E., Fathi K., Wozniak H., Ferruit P., Mundell C. G., Schinnerer E., 2006, *MNRAS*, 365, 367
- Fabian A., 2012, *ARA&A*, 50, 455
- Falcón-Barroso J. et al., 2006, *MNRAS*, 369, 529
- Fathi K., Storchi-Bergmann T., Riffel R. A., Winge C., Axon D. J., Robinson A., Capetti A., Marconi A., 2006, *ApJ*, 641, L25
- Ferrarese L., Ford H., 2005, *Space Sci. Rev.*, 116, 523
- Fischer T. C. et al., 2017, *ApJ*, 834, 30
- Fischer T. C., Crenshaw D. M., Kraemer S. B., Schmitt H. R., Storchi-Bergmann T., Riffel R. A., 2015, *ApJ*, 799, 234
- Fisher D., 1997, *AJ*, 113, 950
- Frank J., King A., Raine D. J., 2002, *Accretion Power in Astrophysics*. Cambridge Univ. Press, Cambridge
- Ganda K., Falcón-Barroso J., Peletier R. F., Cappellari M., Emsellem E., McDermid R. M., de Zeeuw P. T., Carollo C. M., 2006, *MNRAS*, 367, 46
- García-Lorenzo B., Mediavilla E., Arribas S., 1999, *ApJ*, 518, 190
- Gerhard O. E., 1993, *MNRAS*, 265, 213
- Hicks E. K. S., Davies R. I., Malkan M. A., Genzel R., Tacconi L. J., Sánchez F. M., Sternberg A., 2009, *ApJ*, 696, 448
- Hicks E. et al., 2013, *ApJ*, 768, 107
- Jarrett T. H., Chester T., Cutri R., Schneider S. E., Huchra J. P., 2003, *AJ*, 125, 525
- Kormendy J., Ho L. C., 2013, *ARA&A*, 51, 511
- Krajnović D., Cappellari M., de Zeeuw P. T., Copin Y., 2006, *MNRAS*, 366, 787
- Krajnović D. et al., 2011, *MNRAS*, 414, 2993
- Kuijken K., Merrifield M. R., 1995, *ApJ*, 443, L13



- Kuzio de Naray R., Arsenault C. A., Spekkens K., Sellwood J. A., McDonald M., Simon J. D., Teuben P., 2012, *MNRAS*, 427, 2523
- Laine S., Shlosman I., Knapen J. H., Peletier R. F., 2002, *ApJ*, 567, 97
- Lena D. et al., 2015, *ApJ*, 806, 84
- McGregor P. J. et al., 2003, *Proc. SPIE*, 4841, 1581
- Malkan M. A., Gorjian V., Tam R., 1998, *ApJS*, 117, 25
- Maraston C., 2005, *MNRAS*, 362, 799
- Márquez I., Masegosa J., Durret F., González Delgado R. M., Moles M., Maza J., Pérez E., Roth M., 2003, *A&A*, 409, 459
- Martini P., Dicken D., Storchi-Bergmann T., 2013, *MNRAS*, 420, 2249
- Mazzalay X. et al., 2014, *MNRAS*, 438, 2036
- Onken C. et al., 2014, *ApJ*, 791, 37
- Pogge R. W., Martini P., 2002, *ApJ*, 569, 624
- Reese A. S., Williams T. B., Sellwood J. A., Barnes E. I., Powell B. A., 2007, *AJ*, 133, 2846
- Ricci T. V., Steiner J. E., Menezes R. B., 2016, *MNRAS*, 463, 3860
- Riffel R. A., 2010, *Ap&SS*, 327, 239
- Riffel R. A., Storchi-Bergmann T., 2011a, *MNRAS*, 411, 469
- Riffel R. A., Storchi-Bergmann T., 2011b, *MNRAS*, 417, 2752
- Riffel R., Rodríguez-Ardila A., Pastoriza M. G., 2006, *A&A*, 457, 61
- Riffel R. A., Storchi-Bergmann T., Winge C., McGregor P. J., Beck T., Schmitt H., 2008, *MNRAS*, 385, 1129
- Riffel R. A., Storchi-Bergmann T., Riffel R., Pastoriza M. G., 2010, *ApJ*, 713, 469
- Riffel R. A., Storchi-Bergmann T., Nagar N. M., 2010, *MNRAS*, 404, 166
- Riffel R., Riffel R. A., Ferrari F., Storchi-Bergmann T., 2011, *MNRAS*, 416, 493
- Riffel et al., 2013, *MNRAS*, 430, 2249
- Riffel R. A., Storchi-Bergmann T., Riffel R., 2014, *ApJ*, 780, 24
- Riffel R. A. et al., 2015a, *MNRAS*, 446, 2823
- Riffel R. et al., 2015b, *MNRAS*, 450, 3069
- Riffel R. A., Storchi-Bergmann T., Riffel R., 2015c, *MNRAS*, 451, 358
- Sánchez F. M., Davies R. I., Genzel R., Tacconi L. J., Eisenhauer F., Hicks E. K. S., Friedrich S., Sternberg A., 2009, *ApJ*, 691, 749
- Schmitt H. R., Kinney A. L., 2000, *ApJS*, 128, 479
- Schnorr-Müller A., Storchi-Bergmann T., Nagar N. M., Robinson A., Lena D., Riffel R. A., Couto G. S., 2014, *MNRAS*, 437, 1708
- Schnorr-Müller A., Storchi-Bergmann T., Robinson A., Lena D., Nagar N. M., 2016, *MNRAS*, 457, 972
- Schnorr-Müller A., Storchi-Bergmann T., Ferrari F., Nagar N. M., 2017, *MNRAS*, 466, 4370
- Schönell A. J., Riffel R. A., Storchi-Bergmann T., Winge C., 2014, *MNRAS*, 445, 414
- Sellwood J. A., Sánchez R. Z., 2010, *MNRAS*, 404, 1733
- Sellwood J. A., Spekkens K., 2015, preprint ([arXiv:1509.07120](https://arxiv.org/abs/1509.07120))
- Simoes Lopes R. et al., 2007, *ApJ*, 655, 718
- Smajić S., Moser L., Eckart A., Busch G., Combes F., García-Burillo S., Valencia-S. M., Horrobin M., 2015, *A&A*, 583, A104
- Somerville et al., 2008, *MNRAS*, 391, 481
- Spekkens K., Sellwood J. A., 2007, *ApJ*, 664, 204
- Springel et al., 2005, *MNRAS*, 361, 776
- Storchi-Bergmann T., Dors O., Jr, Riffel R. A., Fathi K., Axon D. J., Robinson A., 2007, *ApJ*, 670, 959
- Storchi-Bergmann T., McGregor P., Riffel R. A., Simões Lopes R., Beck T., Dopita M., 2009, *MNRAS*, 394, 1148
- Storchi-Bergmann T., Simões Lopes R., McGregor P., Riffel R. A., Beck T., Martini P., 2010, *MNRAS*, 402, 819
- Storchi-Bergmann T., Riffel R. A., Riffel R., Diniz M., Borges Vale T., McGregor P., 2012, *ApJ*, 755, 87
- Terrazas B. A., Bell E. F., Henriques B. M. B., White S. D. M., Cattaneo A., Woo J., 2016, *ApJ*, 830, L12
- van de Ven G., Fathi K., 2010, *ApJ*, 723, 767
- van der Marel R. P., Franx M., 1993, *ApJ*, 407, 525
- Veilleux S., Tully R. B., Bland-Hawthorn J., 1993, *AJ*, 105, 1318
- Winge C., Riffel R. A., Storchi-Bergmann T., 2009, *ApJS*, 185, 186

## APPENDIX A: STELLAR KINEMATICS BASED ON ALREADY PUBLISHED DATA

Figs A1–A5 show maps for the stellar kinematics of galaxies with previous measurements already published by our group.



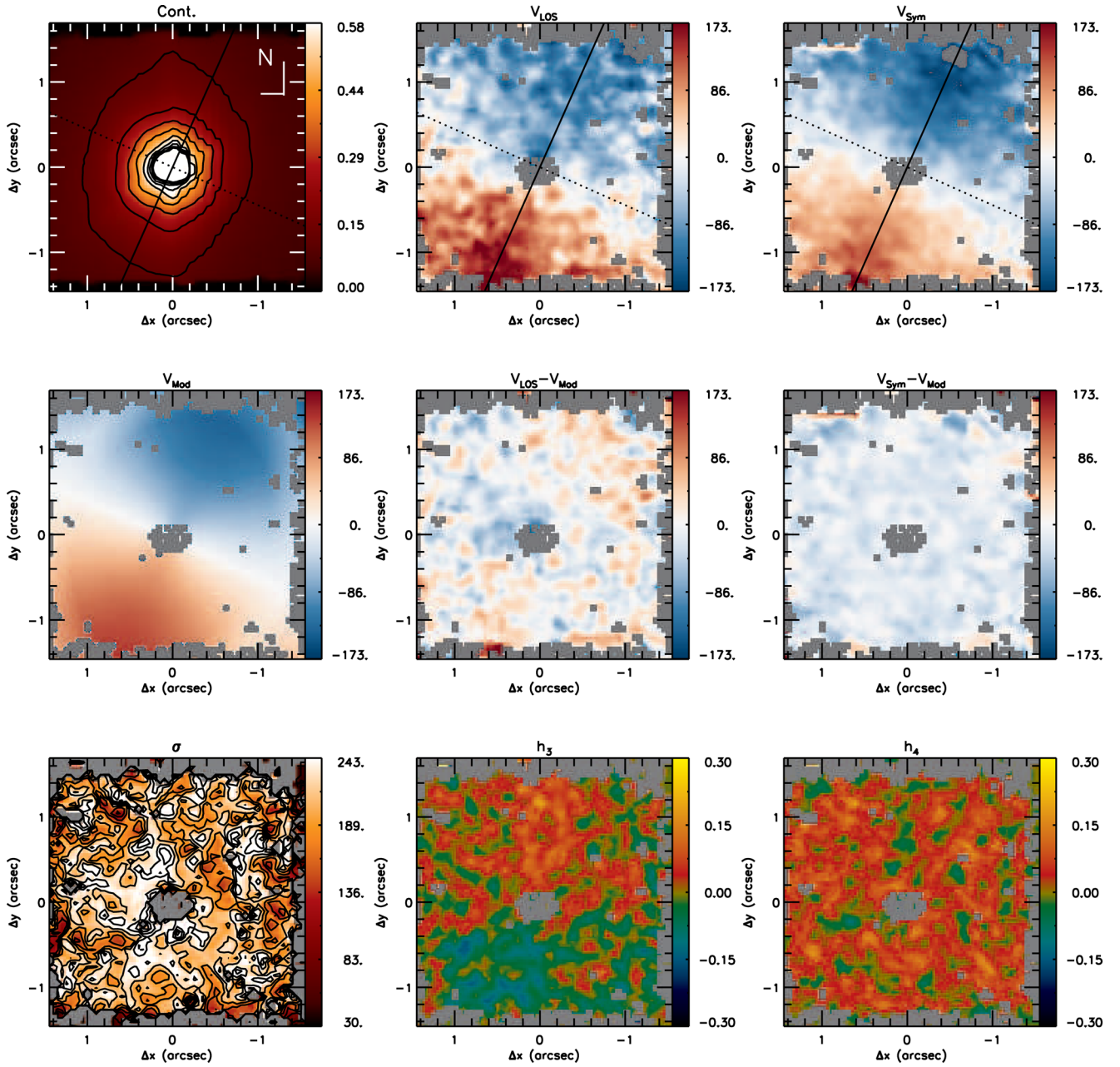


Figure A1. Same as Fig. 2 for NGC 2110. The original stellar kinematics measurements are presented in Diniz et al. (2015).

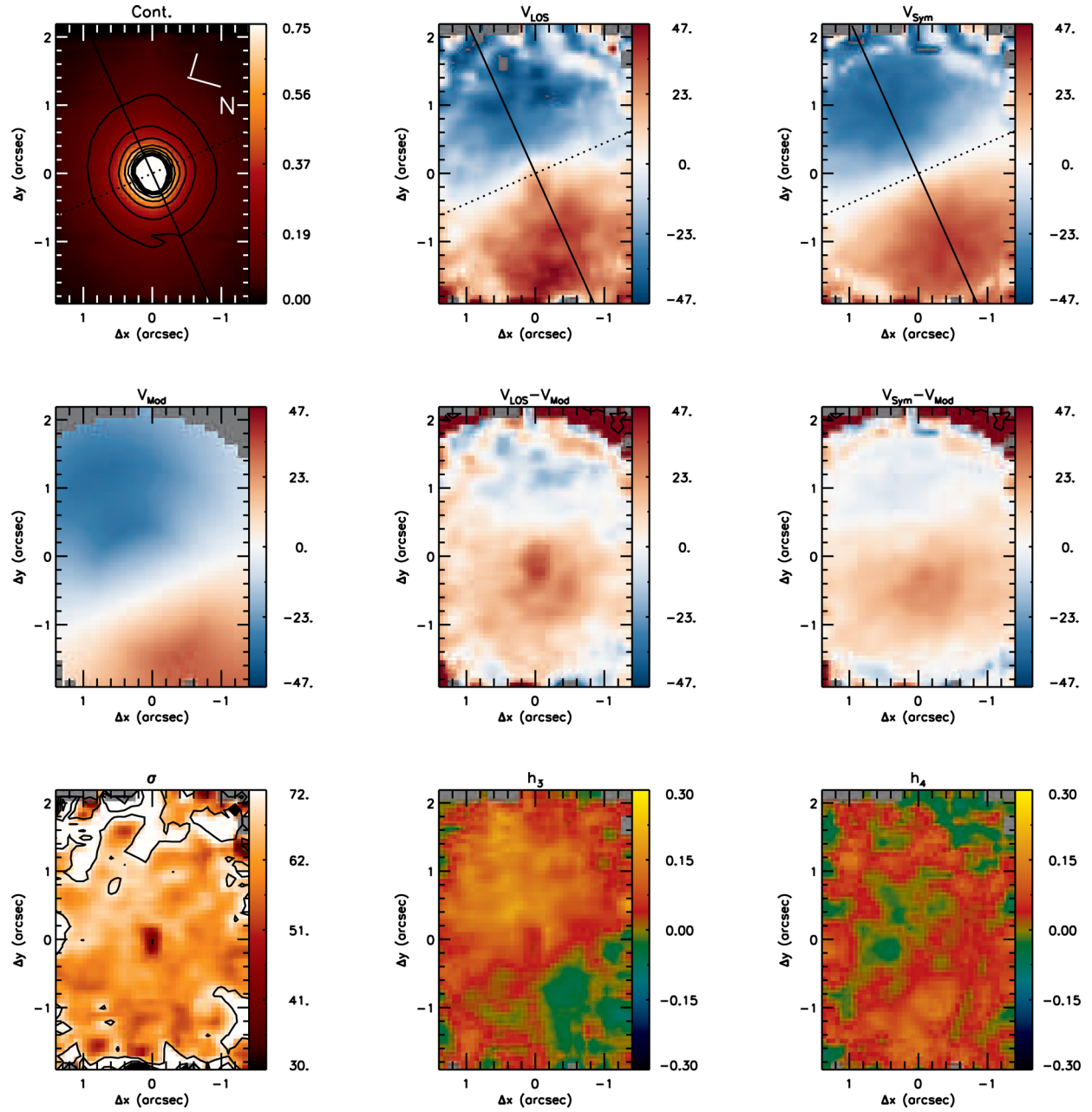


Figure A2. Same as Fig. 2 for NGC 4051. The original stellar kinematics measurements are presented in Riffel et al. (2008).

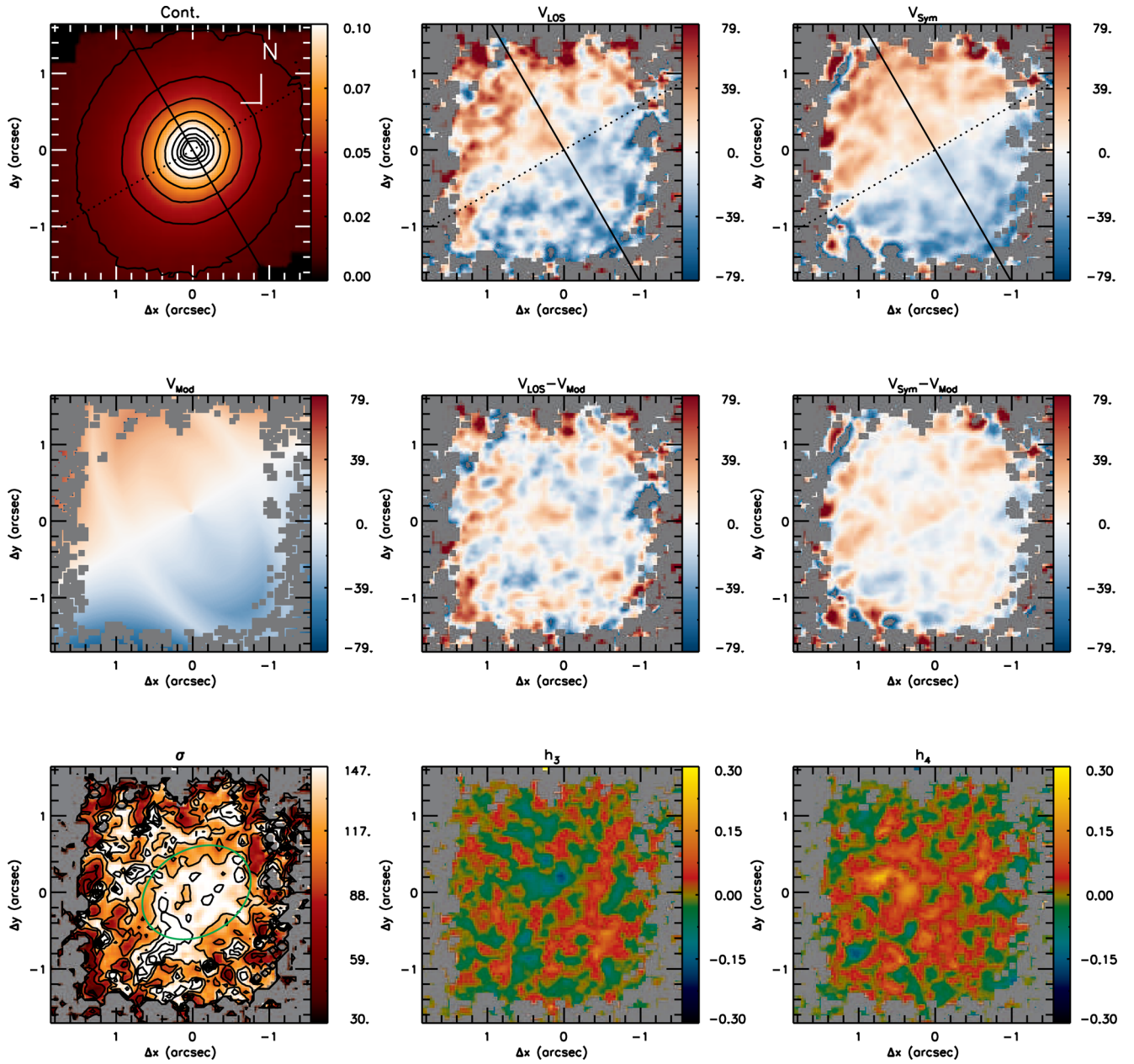
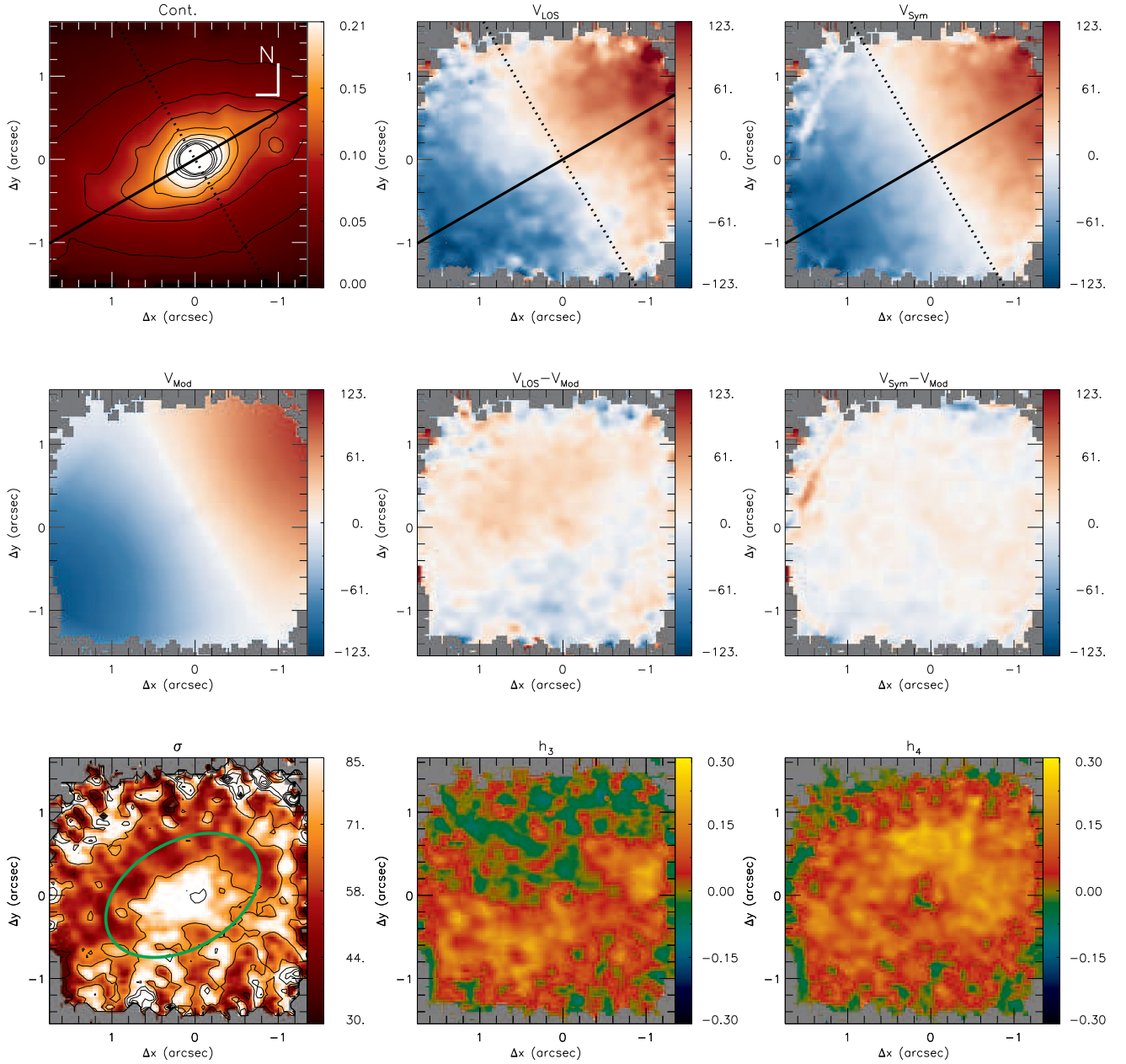
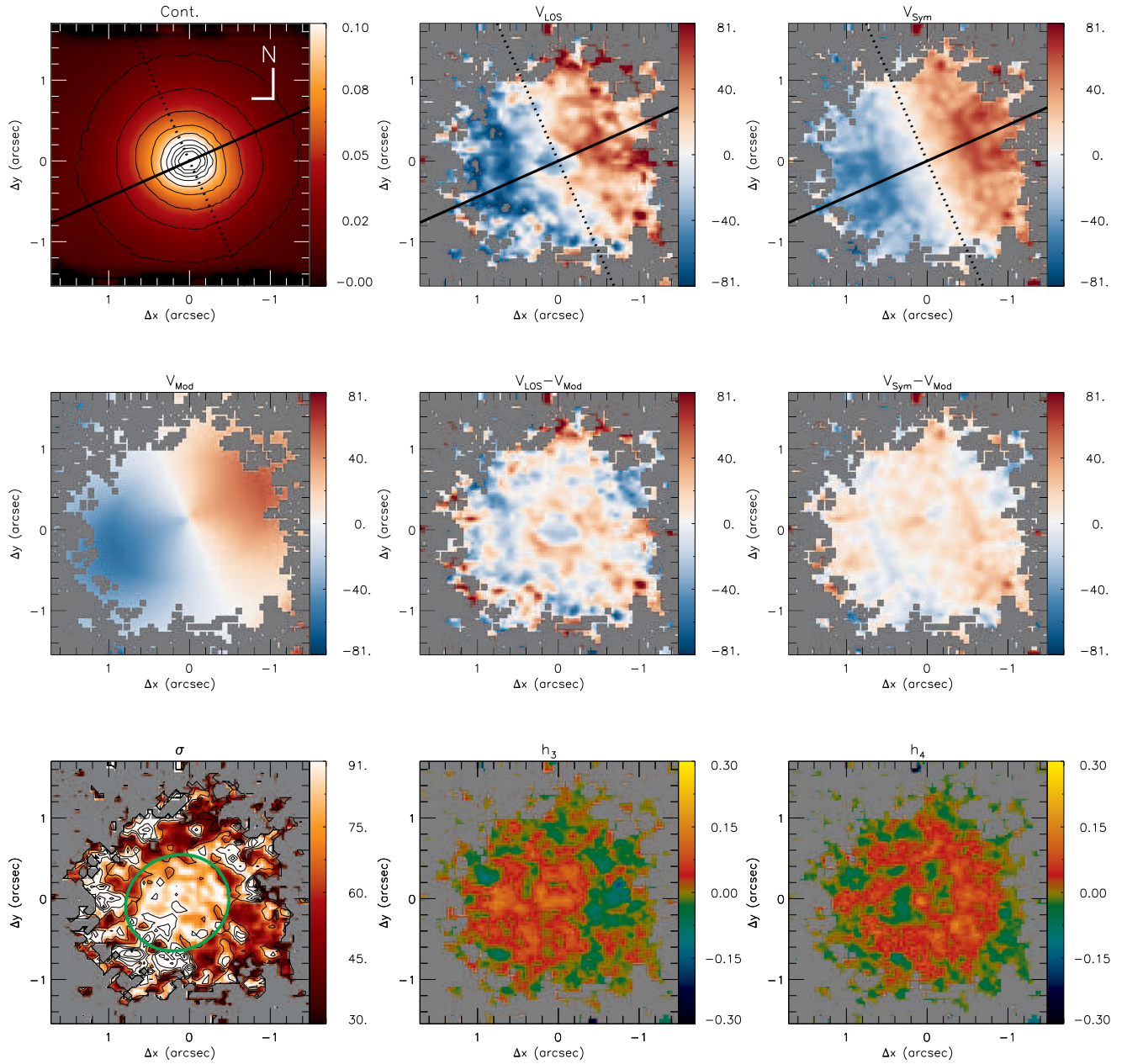


Figure A3. Same as Fig. 2 for NGC 5929. The original stellar kinematics measurements are presented in Riffel et al. (2015c).





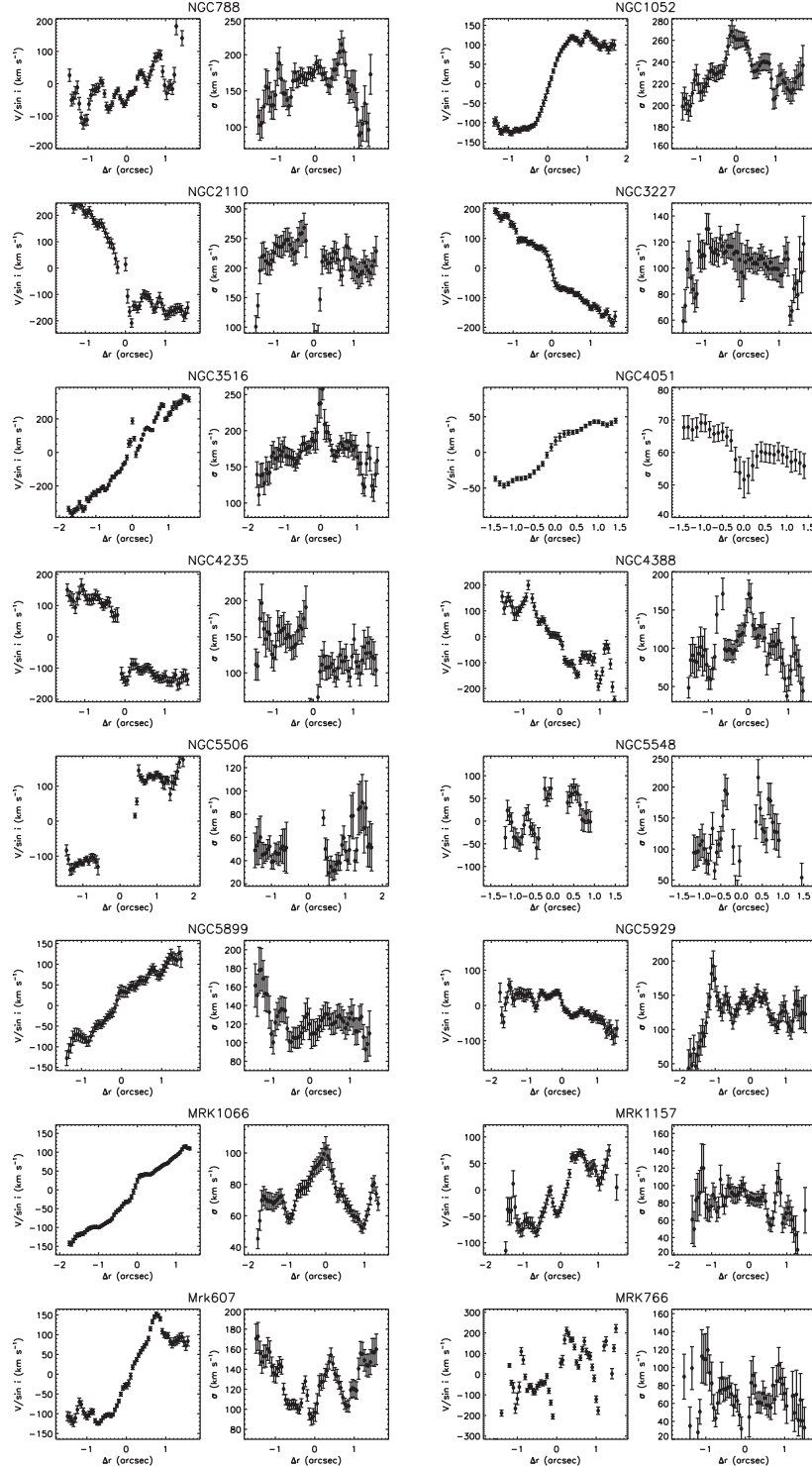
**Figure A4.** Same as Fig. 2 for Mrk 1066. The original stellar kinematic measurements are presented in Riffel & Storchi-Bergmann (2011a).



**Figure A5.** Same as Fig. 2 for Mrk 1157. The original stellar kinematic measurements are presented in Riffel & Storchi-Bergmann (2011b).

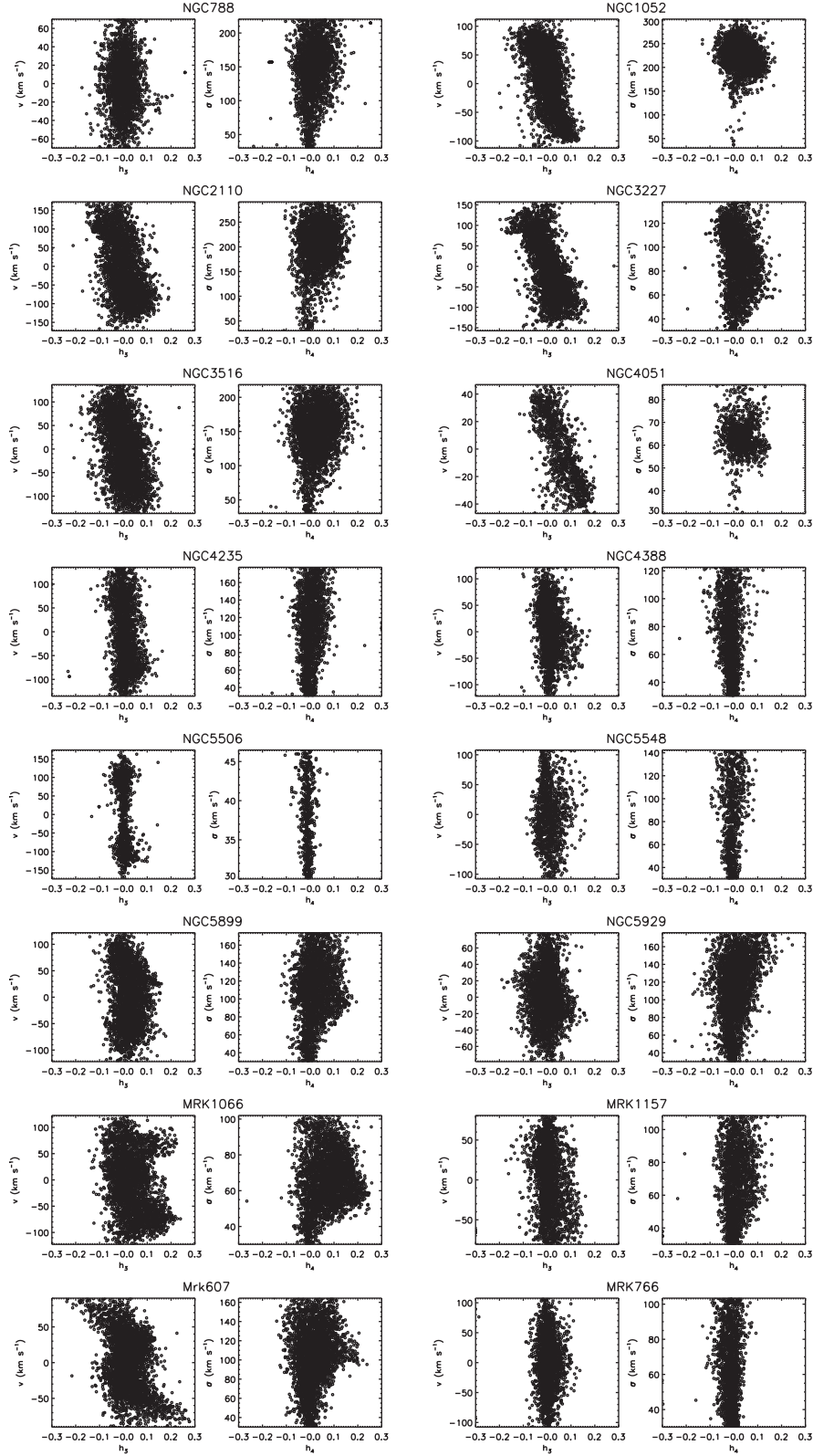
## APPENDIX B: ONE-DIMENSIONAL CUTS FOR THE STELLAR KINEMATICS

Fig. B1 shows one-dimensional cuts along the major axis of the galaxies for the LOS velocity (left) and  $\sigma$  (right). Plots of the LOS velocity ( $V_{\text{LOS}}$ ) versus  $h_3$  and  $\sigma$  versus  $h_4$  using all spaxels are shown in Fig. B2.



**Figure B1.** One-dimensional cuts along the major axis of the galaxies obtained by averaging the observed velocities within a pseudo-slit with 0.25 arcsec width. The orientation of the major axis and the inclination of the disc used in these plots are from Table 2.





**Figure B2.** Plots of the LOS velocity ( $V_{\text{LOS}}$ ) versus  $h_3$  and  $\sigma$  versus  $h_4$  for the galaxies of our sample. For most galaxies,  $V_{\text{LOS}}$  and  $h_3$  are anticorrelated and a trend of higher values of  $\sigma$  being observed at locations with negative  $h_4$  values and smaller  $\sigma$  values associated with positive  $h_4$  values.

This paper has been typeset from a  $\text{\LaTeX}$  file prepared by the author.